



Signal Readout for Transition-Edge Sensor X-ray Imaging Spectrometers

H. Akamatsu, W. B. Doriese, J. A. B. Mates, and B. D. Jackson

Contents

Introduction	2
Basic Concepts of Signal Readout	5
Impedance Matching	5
dc Superconducting Quantum Interference Device (DC-SQUID)	6
Principles of Multiplexed Readout of X-ray TES Microcalorimeters	8
Why Is Multiplexed Readout Necessary?	8
General Considerations	8
Time-Division Multiplexing (TDM)	11
MHz Frequency-Domain Multiplexing (FDM)	19
Microwave-SQUID Multiplexing (μ mux)	27
Summary and Future Prospects	36
Cross-References	39
References	39

Abstract

Arrays of low-temperature microcalorimeters provide a promising technology for X-ray astrophysics: the imaging spectrometer. A camera with at least several thousand pixels, each of which has an energy-resolving power ($E/\Delta E_{\text{FWHM}}$) of

H. Akamatsu (✉)
SRON Netherlands Institute for Space Research, Leiden, The Netherlands
e-mail: h.akamatsu@sron.nl

W. B. Doriese · J. A. B. Mates
United States Department of Commerce, National Institute of Standards and Technology (NIST),
Boulder, CO, USA
e-mail: william.doriese@nist.gov; john.mates@nist.gov

B. D. Jackson
SRON Netherlands Institute for Space Research, Groningen, The Netherlands
e-mail: B.D.Jackson@sron.nl

a few thousand across a broad energy range (200 eV to 10 keV or higher), would be a revolutionary instrument for the study of energetic astrophysical objects and phenomena. Signal readout is a critical enabling technology. Multiplexed readout, in which signals from multiple pixels are combined into a single amplifier channel, allows a kilopixel-scale microcalorimeter array to meet the stringent requirements for power consumption, mass, volume, and cooling capacity in orbit. This chapter describes three different multiplexed-readout technologies for transition-edge sensor microcalorimeters: time-division multiplexing, frequency-domain multiplexing, and microwave-SQUID multiplexing. For each multiplexing technique, we present the basic method, discuss some design considerations and parameters, and show the state of the art. The chapter concludes with a brief discussion of future prospects.

Keywords

X-ray spectrometer · Microcalorimeter · Cryogenic electronics · Signal readout · Multiplexed readout · Semiconductor calorimeter · Transition-edge sensor · Metallic-magnetic calorimeter · SQUID

Introduction

High-energy-resolution X-ray spectroscopy is a powerful probe of elemental and chemical composition that is used across many scientific disciplines, from materials science to the physics of hot plasma in the universe. Wavelength-dispersive (WD) X-ray spectrometers, such as gratings, Bragg crystals, and multilayer materials, can achieve the highest energy-resolving powers ($E/\Delta E \sim 1,000$ to 10,000). WD spectrometers have been deployed previously for X-ray astronomy, such as the Reflection Grating Spectrometer (RGS) on board the XMM-Newton satellite (den Herder et al. 2001) and Chandra's High Energy Transmission Grating Spectrometer (Markert et al. 1994). However, WD spectrometers have important drawbacks for astronomy, such as a limited simultaneous energy range, a low collecting efficiency (solid-angle coverage times quantum efficiency), and a lack of any inherent imaging capability. Another common technology, the solid-state energy-dispersive (ED) detector (e.g., the silicon-drift detector, or SDD, and the charged-coupled device, or CCD), which measures the X-ray energy directly during detection, can combine high collecting efficiency with imaging capability across a wide energy band; however, the energy resolution is limited ($E/\Delta E \leq 50$ @ 6 keV for the best SDDs and somewhat lower for X-ray CCD cameras).

A technology that has been developed over the last few decades for a variety of present and future astronomical missions is the microcalorimeter array (Moseley et al. 1984; McCammon 2005) (see Fig. 1). A microcalorimeter array is an imaging spectrometer that combines some of the best features of WD spectrometers and ED detectors: $E/\Delta E \geq 2,400$ @ 6 keV and a high collecting efficiency. A microcalorimeter pixel consists of a sensitive thermometer and an X-ray absorber

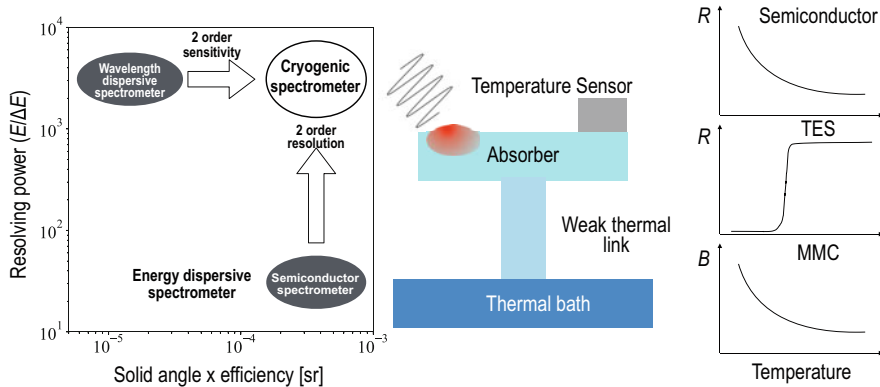


Fig. 1 The microcalorimeter array as a cryogenic imaging spectrometer. *Left*: comparison of cryogenic spectrometers to wavelength-dispersive and solid-state energy-dispersive spectrometers on a plane of energy-resolving power vs. collecting efficiency (Friedrich 2006). Here, collecting efficiency is the solid angle subtended by the spectrometer multiplied by the cumulative quantum efficiency of all components of the spectrometer. *Middle*: cartoon diagram of a single cryogenic microcalorimeter pixel. An X-ray absorber is connected to a thermal bath via a weak thermal link, and also to a thermometer. Measurement of a pulsed change in the absorber temperature yields the energy of the X-ray. *Right, top to bottom*: R vs. T of a semiconductor calorimeter, R vs. T of a transition-edge sensor, and B vs. T of a metallic-magnetic calorimeter

connected weakly to a cryogenic thermal bath. When an X-ray strikes the X-ray absorber, the thermometer measures the magnitude of the resulting temperature pulse to determine the energy of the X-ray.

The energy resolution of a cryogenic spectrometer is estimated as follows:

$$\Delta E \sim \sqrt{\frac{k_B T^2 C}{|\alpha|}}. \quad (1)$$

where k_B , T , C , and $\alpha \equiv d \ln R / d \ln T$ are the Boltzmann constant, detector temperature, heat capacity, and thermometer sensitivity, respectively. The keys to achievement of high-energy-resolving power (low ΔE) are a low operating temperature, a small heat capacity, and a high sensitivity.

While many types of cryogenic thermometers have been proposed and studied, only a few are developed enough to be considered for space-borne instrumentation: semiconductor calorimeters, transition-edge sensors (TESs), and metallic-magnetic calorimeters (MMCs). Table 1 summarizes the basic properties of each type of microcalorimeter, while Table 4 in Section “Summary and Future Prospects” lists present and future missions for each.

The semiconductor calorimeter has a negative thermal coefficient (thermistor R decreases as T increases), a high impedance ($\sim M\Omega$), and a moderate sensitivity ($|\alpha| \sim 7$). Semiconductor calorimeters have been used in many rocket and satellite projects. The X-ray Quantum Calorimeter (XQC) is a sounding-rocket experiment

Table 1 Summary of the three main types of X-ray microcalorimeters: semiconductor, transition-edge sensor (TES), and metallic-magnetic calorimeter (MMC). The upper section lists some basic characteristics of each type of microcalorimeter. Semiconductor microcalorimeters use junction-gate field-effect transistors (JFETs) to read out their voltage, while TESs and MMCs employ superconducting quantum interference devices (SQUIDs) to read out the device current. The lower section gives the best energy resolution achieved in a single pixel and the largest operating detector array (as of the publication of this book)

	Semiconductor	TES	MMC
T of sensor bath [K]	0.05	0.05	0.03
Resistance [Ω]	10^6	0.001 to 1	0.1
Readout amplifier	JFET	SQUID	SQUID
T of readout amplifier [K]	140	0.05	0.03
Multiplexing	Difficult	Highly developed	Possible
Amp. bandwidth	NA	10 MHz (SQUID)	10 MHz
		4 to 8 GHz (HEMT)	
Best ΔE @ 6 keV [eV]	3.7 (Kelley et al. 2008; Porter et al. 2009, 2010)	1.6 (Smith et al. 2012; de Wit et al. 2022)	1.6 (Kempf et al. 2018)
Largest array [pixels]	36 (Ishisaki et al. 2018)	992 (Szypryt et al. 2021b, 2022)	64 (Mantegazzini et al. 2022)

TES transition-edge sensor, *MMC* metallic-magnetic calorimeter, *JFET* junction-gate field-effect transistor, *SQUID* superconducting quantum interference device (see Section “[dc Superconducting Quantum Interference Device \(DC-SQUID\)](#)”), *HEMT* high-electron-mobility transistor (see Section “[Microwave-SQUID Multiplexing \(\$\mu\$ mux\)](#)”)

(McCammon et al. 2002). The ASTRO-E satellite was the first to be equipped with a cryogenic X-ray spectrometer, but it was lost during launch. The ASTRO-E2 Suzaku (Mitsuda et al. 2007) satellite’s XRS (Kelley et al. 2007) was the first microcalorimeter instrument to reach orbit on a satellite, but was lost due to rapid evaporation of the cryogenes. The ASTRO-H Hitomi (Takahashi et al. 2012) satellite’s SXS (Mitsuda et al. 2014) was a pioneer in low-temperature X-ray microcalorimetry and successfully observed X-ray emission from astronomical objects (Hitomi Collaboration et al. 2016); unfortunately, however, the satellite was lost due to a malfunction in its attitude-control system. They will also be employed for the Resolve (Ishisaki et al. 2018) instrument on XRISM (Tashiro et al. 2018). McCammon (2005) gives a detailed review of the technology.

The transition-edge sensor (TES) works in the superconducting transition from the normal to superconducting states, which provides a high-temperature sensitivity ($\alpha \sim 100$). The operating impedance of a TES microcalorimeter ranges from ~ 1 to $10 \text{ m}\Omega$, depending on the TES design and the material chosen for the superconducting film. The sensor is voltage biased and its current is read out via a SQUID. There are several excellent reviews of the TES X-ray microcalorimeter in the literature (Irwin and Hilton 2005; Ullom and Bennett 2015; Gottardi and Nagayashi 2021). TES calorimeters are in use in or planned for many present and future X-ray astronomy projects, including Micro-X (the first TES array and readout system operated in space) (Adams et al. 2020), the X-IFU instrument (Barret et al. 2018) onboard the ESA Athena mission, HUBS (Cui et al. 2020), Super-

DIOS (Sato et al. 2020), and LEM (<https://lem.physics.wisc.edu/>), and the TES is one of the proposed technologies for the Lynx (The Lynx Team 2018) imaging spectrometer (Bandler et al. 2019).

Unlike other resistance calorimeters, the metallic-magnetic calorimeter (MMC) utilizes a non-resistive, paramagnetic temperature sensor; a MMC converts a temperature change into a change in magnetization, which is then measured as a change in magnetic flux in a DC-SQUID (Fleischmann et al. 2005). MMCs have two interesting differences from resistive microcalorimeters: (1) no power is dissipated in the sensor and (2) the readout makes no galvanic contact to the sensor. MMCs also exhibit excellent energy resolution, high dynamic range, and high linearity in their energy-gain scale. MMCs will be used in the International Axion Observatory (Abeln et al. 2021) and are also one of the proposed detector technologies for the Lynx imaging spectrometer (Stevenson et al. 2019).

Because cryogenic X-ray microcalorimeters are formed as small patches of thin films on a silicon substrate, they are naturally fabricated in a two-dimensional array of pixels to create an imaging spectrometer. An international effort is underway to develop large arrays of low-temperature X-ray microcalorimeters. The following two technologies are particularly active areas of research and development:

1. arrays of the scale of 10^4 pixels via microfabrication technology;
2. signal-multiplexing techniques that read out multiple pixels per readout channel, which is necessary to reduce the volume of electronics on the low-temperature (typically about 50 to 100 mK) stage of the spectrometer and the number of wires to that low-temperature stage (see Section “[Why Is Multiplexed Readout Necessary?](#)”).

This chapter presents issues and recent progress in signal-readout technology for arrays of X-ray microcalorimeters.

Basic Concepts of Signal Readout

Impedance Matching

When two circuit elements are connected, such as a microcalorimeter pixel to its readout, a difference in impedance will cause some signal power to be reflected. This loss of signal in the readout decreases the signal-to-noise ratio. This can be compared to exchanging water between two hoses of different diameters: different hose diameters result in water loss.

The following simple calculation illustrates the concept of impedance matching. A signal voltage, V , drives a current, I , through the circuit shown in Fig. 2 (left), given by:

$$I = \frac{V}{R + r}, \quad (2)$$

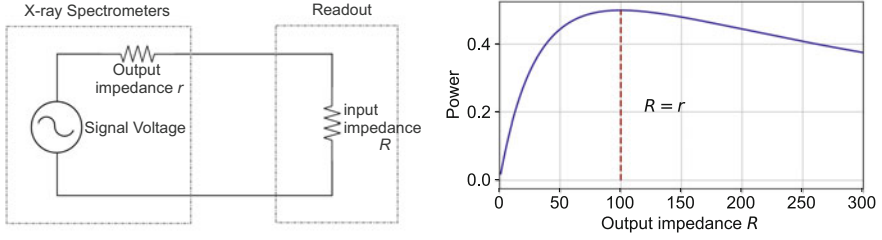


Fig. 2 *Left:* Electrical schematic showing the output impedance, r , of an X-ray microcalorimeter and the input impedance, R , of its readout. *Right:* power transmitted to the readout vs. R for $r = 100 \Omega$. Transmitted power is maximized when the output impedance of the microcalorimeter and the input impedance of the readout electronics are equal

where r and R are the output impedance of an X-ray microcalorimeter pixel and input impedance of its readout, respectively. Therefore, the voltage drop across R is:

$$V_R = RI = V \frac{R}{R + r}. \quad (3)$$

The power dissipated in R , $P_R \equiv IV_R$, and its first derivative with respect to R are:

$$P_R = V^2 \frac{R}{(R + r)^2} \quad \text{and} \quad \frac{dP_R}{dR} = V^2 \frac{r - R}{(R + r)^3}. \quad (4)$$

Thus, power transmission to the readout is maximized ($dP_R/dR = 0$) when the output impedance of the microcalorimeter pixel is equal to the input impedance of the readout (when the impedances are *matched*). Figure 2 (right) plots P_R vs. R for $r = 100 \Omega$.

As shown in Table 1, the various microcalorimeter types have different output impedances, and so require different readout circuits.

dc Superconducting Quantum Interference Device (DC-SQUID)

Superconducting quantum interference devices (SQUIDs) are a class of highly sensitive magnetic sensors that use ring-shaped superconductors containing Josephson junctions to measure extremely weak magnetic fields (Anderson and Rowell 1963; Jaklevic et al. 1964; Chesca et al. 2004). When two superconductors are brought close enough together that their wave functions overlap, a tunnel current flows that is proportional to the phase difference between the two superconducting wave functions. A modern Josephson junction is a sandwich of a few-nanometer-thick insulator or normal-conductive metal between two superconducting films. SQUIDs can reach magnetic field sensitivities as low as $\sim 10^{-15}$ T (Drung et al. 2007); by contrast, the strength of a refrigerator magnet is about 0.02 T, while

the magnetic fields of the human heart and brain are orders of magnitude lower ($\sim 10^{-12}$ T) (Cohen and Givler 1972). There are two main types of SQUIDs: direct current (dc) and radio frequency (rf). The latter are easier to manufacture but are less sensitive because they operate with a single Josephson junction.

The DC-SQUID is a sensitive magnetometer with a wide inherent frequency bandwidth from dc up to the gigahertz range. It has two Josephson junctions in a washer-shaped superconducting loop (see Fig. 3-left). An external magnetic flux applied to the loop drives a screening current that maintains the total flux enclosed by the loop as an integral number of flux quanta (the magnetic flux quantum is $\Phi_0 = h/2e = 2.07 \times 10^{-15}$ Wb, where h is the Planck constant and e is the charge of the electron). This modulates the maximum supercurrent that can flow across the loop periodically, with a period of Φ_0 . When the current through either Josephson junction exceeds its critical current, a voltage develops. The voltage-vs.-current (V - I) curve (see Fig. 3-middle) is thus modulated as a periodic function of the external magnetic field. When the external flux is zero, the phase difference of the superconducting wave functions in the two sides of the SQUID is small (high critical current and thus lower voltage; $\Phi = n\Phi_0$ case, where n is an integer), while when the external magnetic field is close to $(n + 1/2)\Phi_0$, the critical current is suppressed and the generated voltage is higher. When the current bias applied to the device is higher than its highest critical current, the output voltage shows a sinusoidal response to applied magnetic flux.

Series arrays of DC-SQUIDs (Welty and Martinis 1991) are used to increase the voltage gain. Some designs (typically operating at a temperature of 4 K or lower) can approach quantum-limited energy resolution (the energy resolution per bandwidth approaches \hbar).

Parasitic inductances and capacitances in the circuitry of a DC-SQUID can lead to resonances that amplify gigahertz-frequency Josephson oscillations in the

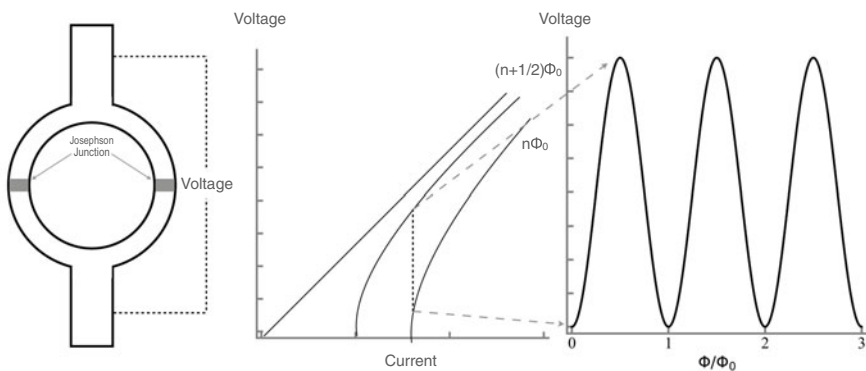


Fig. 3 *Left:* sketch of a DC-SQUID, consisting of two Josephson junctions in a superconducting loop. *Middle:* simulated V vs. I curves in a DC-SQUID for the cases of an integral ($\Phi = n\Phi_0$) and a half-integral ($\Phi = [n + 1/2]\Phi_0$) number of applied flux quanta (n is an integer). *Right:* simulated V vs. Φ curve for a DC-SQUID

SQUID. These resonances can cause undesirable kinks in the otherwise sinusoidal response of the SQUID and excess noise. Careful design, including the use of resistive structures to damp microwave resonances, can reduce or eliminate such behavior (Huber et al. 1997, 2001).

Principles of Multiplexed Readout of X-ray TES Microcalorimeters

Why Is Multiplexed Readout Necessary?

X-ray astronomy differs significantly from other fields in that X-ray signals from celestial objects do not reach the ground due to atmospheric absorption. Thus, X-ray observatories (and also, generally, gamma-ray observatories) *must* be placed on space-borne platforms such as rockets and satellites.

Low-temperature microcalorimeters make excellent X-ray imaging spectrometers, as described by Gottardi and Smith in this book. However, readout of large arrays of microcalorimeters is nontrivial due to the electrical power and cooling capacity available in a satellite. For example, the total electrical draw of a typical communication satellite is about 1 to 1.5 kW (https://www.esa.int/Enabling_Support/Space_Engineering_Technology/Power_Systems) (about the same as a standard household microwave oven), while the Hubble Space Telescope uses about 2.8 kW (<https://www.nasa.gov/content/goddard/hubble-space-telescope-electrical-power-system>). For X-ray astronomy, the Athena satellite has a planned power draw of ~ 6 kW, of which the X-IFU instrument will draw about 1.3 kW (Ravera et al. 2014).

As discussed in Fig. 4, readout of a single TES microcalorimeter pixel requires a minimum of three cryogenic wire pairs, while five pairs per TES are typical. Thus, brute-force readout of X-IFU's $\sim 2,400$ TESs (Barret et al. 2018) would require more than 10,000 wire pairs. The power draw from 2,400 channels of room-temperature electronics plus a cryogenic system capable of overcoming the thermal conductivity of this many wires would overwhelm any feasible satellite platform. Future arrays of X-ray microcalorimeters will be even larger. To solve this problem, signal-multiplexing techniques that read signals from multiple sensors with fewer wires are essential.

General Considerations

Multiplexed readout should introduce minimal noise and signal degradation. The noise budget is application-dependent: e.g., in Athena X-IFU, about 3% of the energy-resolution budget is allocated to readout. Successful multiplexing generally entails these three considerations:

- 1. The signal and noise bandwidths of the sensor should be made as narrow as feasible for the astronomical application.** The signal and noise currents of TES X-ray microcalorimeters generally obey two low-pass time constants: the electrical time constant (determines behavior on the leading edge of an X-ray pulse) and the

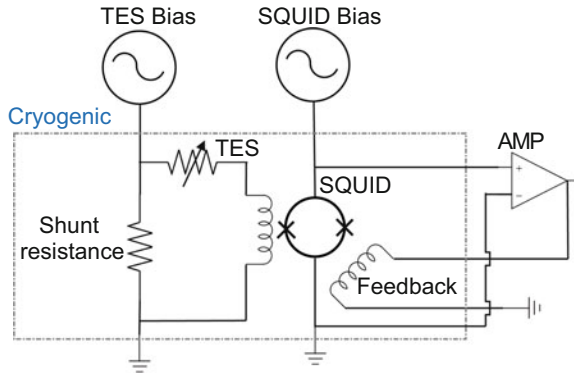


Fig. 4 Schematic of the readout of a TES via a single-stage DC-SQUID. Cryogenic components are inside the dashed box. This is the simplest reasonable implementation of (non-multiplexed) readout of a TES and requires three cryogenic wire pairs per TES (for TES bias, SQUID bias/output, and SQUID feedback). However, typically, a two-stage SQUID architecture is needed to achieve the required gain without dissipation of too much Joule power on the coldest cryogenic stage (see Fig. 7); in this case, at least five cryogenic wire pairs per TES are needed

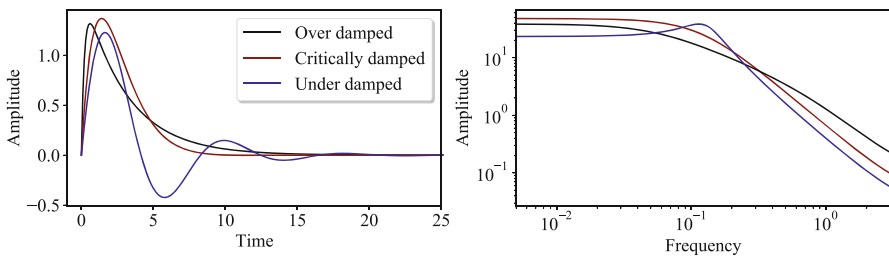


Fig. 5 Simulated TES-current pulses (left: current vs. time; right: current*time vs. frequency) under various damping conditions. In the overdamped condition, the relation between the TES time constants is $\tau_{\text{rise}} < \tau_{\text{decay}}$ (and both are real). In a critically damped pulse, $\tau_{\text{rise}} = \tau_{\text{decay}}$. In an underdamped pulse, the time constants are complex conjugates

thermal time constant (determines the pulse's decay behavior). Irwin and Hilton (2005) discuss the theory of TES signals, including how electrothermal feedback (ETF) governs the interaction between the electrical and thermal time constants. Here, we refer to the TES's ETF-modified time constants on the leading and falling edges of a pulse as τ_{rise} and τ_{decay} , respectively. The achievable X-ray count rate is governed by τ_{decay} : a faster-decaying detector exhibits less pulse pileup for a given input rate of X-rays. The signal bandwidth of the TES is governed by τ_{rise} . The ratio between τ_{rise} and τ_{decay} is generally adjusted via inductance in the TES-bias loop (see, e.g., L_{Ny} in Fig. 7). Figure 5 shows simulated TES-current pulses under various damping conditions. The critically damped (or just a bit overdamped) condition is often the design goal for the TES-bias circuit: for a given TES model, critical damping provides the largest τ_{rise} , and thus the narrowest overall signal bandwidth, and so is often preferred for multiplexed readout. Also, because τ_{rise}

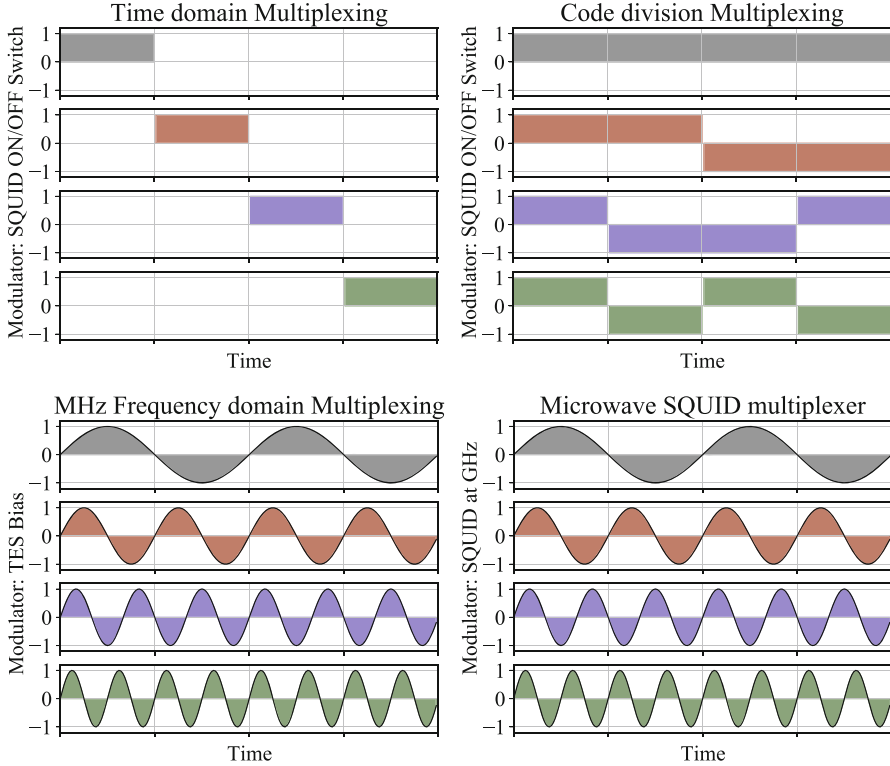


Fig. 6 Multiplexer modulation functions vs. time for the basis vectors of four-channel versions of time-division (TDM), code-division (CDM), MHz-band frequency-domain (FDM), and microwave-SQUID multiplexing (μ mux). Colors indicate the different pixels. Modulation in TDM is via switching SQUIDs on and off, so the basis set is the identity matrix. In CDM, TESs are coupled to different SQUIDs with different polarities to create orthogonal Walsh codes. In FDM, different TESs are biased at different megahertz frequencies. In μ mux, different rf SQUIDs are biased at different gigahertz frequencies. Both FDM and μ mux thus use sine waves to form their orthogonal basis sets

cannot be longer than τ_{decay} , per-pixel X-ray counting capability is in natural tension with multiplexing factor (and thus with array size). Finally, filtering limits sensor noise from being aliased within a multiplexer pixel or from leaking into neighboring multiplexer pixels: the TES-current noise due to phonon exchange with the bath is low-pass filtered with the time constants τ_{decay} and τ_{rise} , while the TES-Johnson noise is low-pass filtered with the time constant τ_{rise} .

2. The readout system should have a wide bandwidth. Multiplexed readout is essentially an exercise in stuffing many low-bandwidth TES signals into a high-bandwidth readout system. Higher readout bandwidth generally allows more TESs per readout channel.

3. The multiplexer should be built from an orthogonal basis set to prevent signal leakage from pixel to pixel. Figure 6 shows the basis sets used by the main multiplexing techniques for TESs to be discussed

in Sections “[Time-Division Multiplexing \(TDM\)](#)”, “[MHz Frequency-Domain Multiplexing \(FDM\)](#)”, and “[Microwave-SQUID Multiplexing \(\$\mu\$ mux\)](#)”: time-division multiplexing (TDM), frequency-domain multiplexing (FDM), and microwave-SQUID multiplexing (μ mux). In addition, this figure shows the basis set of code-division multiplexing (CDM) (Irwin et al. 2010, 2012; Morgan et al. 2016; Doriese et al. 2019; Yu et al. 2020). Irwin (2009) discusses, in the context of information theory, the number of pixels that can be multiplexed via the various techniques. A summary of these techniques is given in Table 2.

TDM and μ mux for TESs are under development by the Quantum Sensors Group at NIST’s Boulder Labs. FDM for TESs was initially demonstrated (Cunningham et al. 2002) by a team from Lawrence Livermore National Lab, UC Berkeley, and Lawrence Berkeley National Lab, and is under development by UC Berkeley, McGill University, and SRON. CDM for TESs was pursued by NIST as an early option for Athena X-IFU and Lynx, but is not presently under development for any mission and so is not discussed further in this chapter. MMCs can be read out via μ mux (Wegner et al. 2018).

Time-Division Multiplexing (TDM)

In the time-division multiplexing (TDM) technique, each TES has its own first-stage DC-SQUID (SQ1). The TESs are dc-biased and are always on, while the SQ1s are turned on and off such that one SQ1 is on at a time per readout column (In TDM, an amplifier chain is usually referred to as a readout “column.” Throughout this chapter, we use the terms “amplifier chain,” “readout channel,” “multiplexer channel,” and “readout column” interchangeably to refer to the logical readout unit that is divided into detector pixels via multiplexing.). Only the signal current from the TES whose SQ1 is on is read out, instantaneously, by the column.

The TDM scheme was proposed in 1999 (Chervenak et al. 1999) for the readout of arrays of TES bolometers and microcalorimeters for various astronomical applications. In the 20+ years since, several TDM-based bolometric arrays (Holland et al. 2013; Swetz et al. 2011; Harper et al. 2018; Gandilo et al. 2016), each of the kilopixel to multi-kilopixel scale, have been deployed for far-IR, millimeter-wave, and submillimeter-wave astronomy. In addition, about 15 TDM-based X-ray spectrometers (Doriese et al. 2017; Yamada et al. 2021; Lee et al. 2019), each of the few-hundred-pixel scale (to be discussed further in Section “[Laboratory TDM Systems](#)”), have been deployed to X-ray-science facilities around the world. A 128-pixel TDM X-ray array flew on the Micro-X sounding rocket in 2018 (Adams et al. 2021) and again in August 2022. Presently, TDM is undergoing refinement (Smith et al. 2021; Durkin et al. 2021) for the multi-kilopixel X-IFU imaging spectrometer for ESA’s Athena mission (see Section “[Optimizations for Space Flight: Athena X-IFU](#)”).

How does TDM compare to the other main multiplexing technologies for TES microcalorimeters, philosophically and at the systems level? Philosophically, in TDM, the SQ1s are the modulated elements, while the TESs themselves are not modulated; this is the same as in the microwave-multiplexing (μ mux;

Table 2 Summary information for four multiplexed-readout technologies for TESs X-ray calorimeters: time-division (TDM), code-division (CDM), MHz-frequency-division (FDM), and microwave-SQUID (μ mux) multiplexing. The top section lists the type of TES bias and the type of modulation. The second section discusses the front-end SQUID. The third section discusses the second-stage amplifier; in μ mux readout, a high-electron-mobility transistor (HEMT) amplifier is traditionally used, but the recently developed kinetic-inductance traveling-wave parametric amplifier (KITWPA) offers an attractive lower-power alternative. Finally, the fourth section lists the state of the art in the readout of X-ray-TES arrays

	TDM (Chervenak et al. 1999; Durkin et al. 2021)	CDM (Irwin et al. 2010; Morgan et al. 2016)	MHz FDM (Yoon et al. 2001; Kiviranta et al. 2002)	μ mux (Irwin and Lehnert 2004; Mates et al. 2008)
TES bias	dc	dc	ac	dc
How modulated?	SQUIDs on/off	Walsh codes (Walsh 1923)	Resonating TESs	resonating SQUIDs
Front-end SQUID	dc	dc	dc	rf
FE SQ: P_{Joule}	450 pW (Durkin et al. 2020)	450 pW (Doriese et al. 2019)	450 pW (Kiviranta et al. 2021)	20 pW
Second-stage amplifier	SQUID array	SQUID array	SQUID array	HEMT (Duh et al. 1988)
Second stage: $P @ T$	~ 300 nW @ 2 K	~ 300 nW @ 2 K	~ 300 nW @ 2 K	~ 5 mW @ 4 K KITWPA (Malnou et al. 2022) (0.2 to 20) μ W @ 4 K ^a
Demonstrated $\Delta E_{\text{FWHM}} @ E @ \text{channels} \times \text{mux factor}$	2.23 eV @ 6 keV @ 1×40 (Durkin et al. 2019) 1.98 eV @ 6 keV @ 8×32 (Smith et al. 2021)	2.77 eV @ 6 keV @ 1×32 (Morgan et al. 2016)	2.23 eV @ 6 keV @ 1×37 (Akamatsu et al. 2021) 2.14 eV @ 6 keV @ 1×31 (Akamatsu et al. 2021)	3.3 eV @ 6 keV @ 1×37 (Nakashima et al. 2020) 3.4 eV @ 6 keV @ 1×28 (Yoon et al. 2018) 2.04 eV @ 1.25 keV @ 1×88 (Bennett et al. 2019) 10 eV @ 6 ^b keV @ $4 \times \sim 210$ [pre-pub comm.]

^aKITWPA power dissipation depends on pump power and therefore scales with compression point of the amplifier

^bTOMCAT (Szypryt et al. 2021a) TESs were optimized for very high count rates and not for energy resolution

Section “[Microwave-SQUID Multiplexing \(\$\mu\text{mux}\$ \)](#)”) scheme, while the frequency-domain scheme (FDM; Section “[MHz Frequency-Domain Multiplexing \(FDM\)](#)”) takes the opposite approach. At the systems level, in TDM the cryogenic electronics are the most complicated, followed by those in μmux and then FDM, while the TDM room-temperature electronics are simpler than those of either FDM or μmux .

Principles of TDM Operation

Figure 7 shows circuit diagrams that contain the building blocks of a TDM readout system. Figure 7a shows readout of a single dc-biased TES by two stages of DC-SQUIDs (see Fig. 3). The signal of interest in a TES X-ray microcalorimeter is its current, which is modulated as a pulsed decrement by each incident X-ray; the amplitude of the TES-current pulse is roughly proportional to the energy of the X-ray. A change in the TES current modulates the flux in the first-stage DC-SQUID (SQ1), which in turn modulates the SQ1 bias current. The current-biased SQUID-series-array (Huber et al. 1997, 2001) (SSA) amplifies the SQ1 current to a voltage at the SSA output, which is amplified further by a room-temperature low-noise amplifier (LNA).

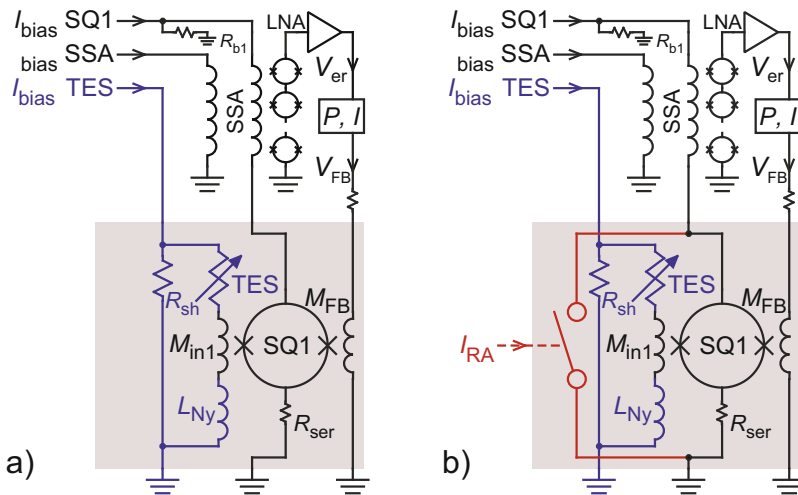


Fig. 7 Readout of a dc-biased TES by a DC-SQUID chain. (a) A single TES under dc bias is read out by a first-stage DC-SQUID (SQ1) and a series array of DC-SQUIDs (SSA). The signal of interest, the TES current, is converted to flux in SQ1 via its input coil (M_{in1}). The SSA reads out the SQ1 current in the same manner. The elements in the gray box are located on the same temperature stage as the TES, which for X-ray TESs, it is typically around 50 mK. TES-related circuit elements (the TES-shunt resistor, or R_{sh} , and the bandwidth-limiting Nyquist inductor, or L_{Ny}) are in blue, while the SQUID-related circuit elements are in black. The SSA is usually located at a higher-temperature cryogenic stage to accommodate its Joule-power dissipation. (b) The same circuit diagram as (a), but with the addition of a superconducting switch (red) to turn on and off the SQ1. When the switch is closed, the SQ1-bias current bypasses SQ1, so the TES-signal current is not transmitted up the readout chain. When the switch is open, circuit (b) behaves like circuit (a)

Because the (quasi-sinusoidal) transfer function of the combined V - Φ curve of the SQ1 and the SSA is highly nonlinear, the readout is run as a flux-locked loop (FLL) to linearize the response. Thus, the “output” signal of this readout system is the feedback voltage, V_{FB} , that is applied to null the TES-signal current to maintain a constant flux in its SQ1.

Figure 7b shows the addition of a superconducting switch to turn on and off the SQ1. The switch chosen for modern TDM implementations (Beyer and Drung 2008; Doriese et al. 2016) is based on the DC-SQUID-like Zappe interferometer (Zappe 1977). An interferometer element consists of several Josephson junctions in parallel (with the number of junctions varying across implementations). The “row-address” (RA) current (I_{RA}) is coupled to the SQUID loops such that with $I_{\text{RA}} = 0$ the interferometer acts as a superconducting wire (the switch is “closed”), while with $I_{\text{RA}} = \Phi_0/2$ the junctions are perfectly out of phase and the nominal current-carrying capacity of the interferometer is zero (the switch is “open”). In the NIST implementation (Irwin et al. 2012), each interferometer element contains four junctions with equal critical currents for ease of fabrication and wide operating margins. Tens of these interferometric elements are wired in series to create an operating dynamic resistance of this “flux-actuated switch” (FAS) that is much larger than that of the signal SQ1.

Figure 8 (left) shows a cartoon circuit schematic of a two-column \times two-row TDM system. In a general M -column \times N -row array of TESs, both the count of cryogenic wires and the number of amplifier chains would scale as MN under brute-force (non-multiplexed) readout; with TDM readout, these scale only as $\sim (M + N)$ and M , respectively. These savings in channels and wires are the main reason to use a multiplexed-readout scheme.

Rows of SQ1s are sequentially turned on via application of a RA current (I_{RA}) to their FASs. TDM columns are read out in parallel. The signal from one TES at a time per column is passed to that column’s SSA. During a row, the LNA’s output voltage, or error signal (V_{er}), is digitally sampled, and then the proportional-integral (P, I) flux-feedback signal (V_{FB}) that would servo the row’s V_{er} to a constant value is digitally calculated and stored to be applied inductively (via M_{FB}) on the digital FLL’s next visit to the row. The digital-readout electronics (DRE; to be discussed further in Section “Room-Temperature Electronics”) synchronize the RA and D-FLL signals and stream the TES-current data to the back-end processor. The TDM system samples each TES once per frame time ($t_{\text{fr}} = t_{\text{row}}N_{\text{rows}}$); if the frame time is short compared to the time constants of the TES-current signals, then the system can reconstruct each TES’s current with high fidelity. Figure 8 (right) shows the multiplexed time streams of the flux-feedback signals of the two two-pixel TDM columns.

Circuit Parameters, Multiplexing Factor, and Noise Scaling

For the dimensioning of a TDM system, an important characteristic of the TES signal-current (I_{TES}) is its slew rate. The highest required TES-current slew rate, \dot{I}_{max} , will occur at the leading edge of an X-ray pulse and is a function of the TES design and its bias-circuit inductance and the highest X-ray energy of interest. If

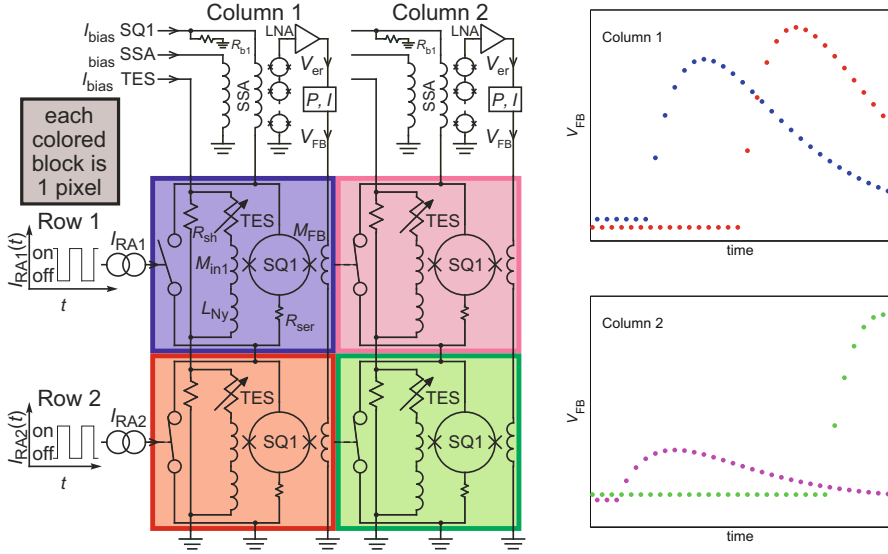


Fig. 8 (left) Schematic of a two-column by two-row TDM. Each colored block is a unit pixel and contains the same cryogenic components as shown in the gray box in Fig. 7b. Rows of SQ1s are sequentially turned on via application of a row-address current (I_{RA}) to their flux-actuated switches. Thus, only one TES at a time per column is read out. To keep the nonlinear, two-stage SQUID amplifier in a quasi-linear range, each column is run as a set of digitally interleaved flux-locked loops. (right) Color-coded, simulated data streams showing the interleaved V_{FB} signals for Columns 1 and 2 as the four TESs respond in current pulses to X-ray events

the D-FLL system is to function correctly, the flux difference in any SQ1 from one sample to the next, injected into M_{in1} by I_{TES} , must result in an error signal that remains within a quasi-linear region of the combined SQ1-SSA $V-\Phi$ curve (see Fig. 3 for an example curve). Thus, the flux difference must obey $\Delta\Phi \leq F\Phi_0$. The fraction, F , of the flux quantum over which the SQUID curve is roughly linear depends on the details of the SQUID designs and is usually between 0.2 and 0.5. The flux difference between frames is $\Delta\Phi = \dot{I}M_{in1}t_{fr}$. Thus (Doriese et al. 2006),

$$\dot{I}_{max}M_{in1}t_{row}N_{rows} \leq F\Phi_0 \quad (5)$$

sets a joint condition on M_{in1} and N_{rows} . If all else is equal, a larger multiplexing factor requires a proportionally smaller input coupling of TES current to SQ1 flux.

The second important consideration in dimensioning a TDM system is readout noise. A given TES X-ray microcalorimeter design will have a value of the spectral density of (white) multiplexed-readout noise ($\sqrt{S_{I-mux}}$; referred to the TES current; units of A/\sqrt{Hz}) above which it is unable to meet the mission/experimental specification on energy resolution. A goal of the system design, then, is to keep $\sqrt{S_{I-mux}}$ below this maximum-allowed value. The SQUID-amplifier system's noise (including contributions from both stages of DC-SQUIDS and the room-temperature

electronics) is approximated as being white (with spectral density $\sqrt{S_\Phi}$; referred to SQ1 flux; units of $\Phi_0/\sqrt{\text{Hz}}$) out to a high-frequency, with a single-pole, low-pass rolloff with time constant τ_{OL} . In a modern TDM system (Doriese et al. 2016), values of $\sqrt{S_\Phi} = 0.2 \mu\Phi_0/\sqrt{\text{Hz}}$ and $f_{\text{OL}} \sim 8$ to 10 MHz are reasonable. The large open-loop bandwidth, f_{OL} , needed to switch quickly from row to row in TDM, combined with the readout strategy that samples each row only once per frame, means the Nyquist anti-aliasing criterion, $1/t_{\text{fr}} \geq 2f_{\text{OL}}$, is not met for the readout noise. As a result, high-frequency amplifier noise is aliased into the TES-signal band. This noise aliasing is an inherent condition of the TDM method and is generally what limits the multiplexing factor for a given application. The TES-referred, multiplexed readout-noise level is given by (Doriese et al. 2006):

$$\sqrt{S_{I-\text{mux}}} = \sqrt{AN_{\text{rows}}S_\Phi/M_{\text{in1}}}. \quad (6)$$

Here, $A \geq 1$ is an alias-scaling factor that depends on the digital-sampling strategy and the ratio $t_{\text{row}}/\tau_{\text{OL}}$. For the common operational case in which $t_{\text{row}} \sim 2\pi\tau_{\text{OL}}$ and the digital sampling occupies a small fraction of t_{row} at the end of the row period (Doriese et al. 2006), $A \sim \pi$. In the limit of $f_{\text{OL}} \rightarrow \infty$, in which the digital sampling can occupy the full row period, $A \rightarrow 1$. In both the modern lab systems (see Section “Laboratory TDM Systems”) and the proposed design of Athena X-IFU (see Section “Optimizations for Space Flight: Athena X-IFU”), the row time is chosen to be $t_{\text{row}} = 160$ ns; this is well matched to the achievable open-loop bandwidth in standard dc-coupled twisted-pair and flexible-microstrip circuits of $f_{\text{OL}} \sim 8$ to 10 MHz.

Equation 6 shows that the TES-referred readout noise scales as $\sqrt{N_{\text{rows}}}/M_{\text{in1}}$, while Eq. 5 shows that M_{in1} scales as $1/N_{\text{rows}}$. Thus, in a TDM system, TES-referred readout noise scales with the multiplexing factor as $\sqrt{S_{I-\text{mux}}} \propto N_{\text{rows}}^{3/2}$.

Room-Temperature Electronics

The room-temperature electronics for TDM readout separate neatly into two functional pieces: the warm-front-end electronics (WFEE) and the digital-readout electronics (DRE).

The WFEE contains the LNA and generates various low-frequency analog-bias signals for the SQUIDs and TESs. Because the pre-LNA SSA-output signals are small (a few millivolts) and thus EMI-sensitive, the WFEE often shares a Faraday cage with the cryostat. For high-performance TDM readout of TES X-ray microcalorimeters, the LNA is challenging to implement. Its needed specifications are $f_{\text{OL}} \geq 10$ MHz and input-voltage noise below $1 \text{ nV}/\sqrt{\text{Hz}}$; this combination is on the edge of what is available in commercial op-amps, so the front end of the LNA is often assembled from discrete transistors. Various groups have produced WFEE modules that have been used for TDM readout over the last 20+ years (Battistelli et al. 2008; Drung et al. 2005; Reintsema et al. 2003; Doriese et al. 2016; Sakai et al. 2022; Gonzales et al. 2022).

The DRE generates the fast RA signals to drive the FASs and runs the D-FLL for each column. In most ground-based applications, raw D-FLL data are streamed to a host computer for demultiplexing, triggering, filtering, and other signal processing; however, on Athena X-IFU, these higher-level functions will be performed within the DRE. Various versions of TDM-DRE have been produced and used over the last 20+ years (Battistelli et al. 2008; Reintsema et al. 2003, 2009; Sakai et al. 2022).

Laboratory TDM Systems

Between 2010 and 2022, the NIST Quantum Sensors Group (Boulder, CO, USA) has deployed about 15 TDM-based TES-microcalorimeter arrays to various X-ray-spectroscopy experiments and facilities around the world (Doriese et al. 2017). This development effort has allowed TDM technology to be tested in real-world conditions beyond the traditional environment of the detector lab. Application areas have included time-resolved absorption and emission spectroscopy with a tabletop, broad-band source (Uhlir et al. 2013; Miaja-Avila et al. 2016; O’Neil et al. 2017), synchrotron-based X-ray-emission and absorption spectroscopy (Yamada et al. 2021; Lee et al. 2019), synchrotron-based energy-resolved scattering (Lee et al. 2022), particle-induced X-ray-emission spectroscopy (Palosaari et al. 2016), spectroscopy of hadronic and muonic atoms (Hashimoto et al. 2022; Okumura et al. 2021), the metrology of X-ray-line energies (Fowler et al. 2021; Szypryt et al. 2019), and X-ray tomography of integrated circuits (Szypryt et al. 2021b). Similar arrays of gamma-ray TESs have been used for the assay of special-nuclear materials (Bennett et al. 2012).

The NIST lab TDM system for X-ray TESs accommodates up to 8 TDM columns and up to 32 TDM rows (up to 256 TES pixels). The heart of each spectrometer is the 50 mK “snout” package (see Fig. 9). This package contains the TES array, the biasing circuitry for the TESs (blue components in Fig. 7), and the SQ1s and FASs.

The 8x32 TDM snout system has also been used to develop TDM readout to meet the stringent performance requirements for Athena’s X-IFU. As Fig. 10 illustrates, by late 2019, TDM had achieved the needed performance for X-IFU.

Optimizations for Space Flight: Athena X-IFU

TDM has been improved in three significant ways from its 8x32-lab configuration (Doriese et al. 2016, 2017) to optimize it for Athena X-IFU.

The first optimization was to increase the open-loop bandwidth in the link between the SQ1s and the SSA. This bandwidth is $R_{\text{dyn}}/(2\pi L_{\text{tot}})$, and for X-IFU, the desired value is 15 MHz (12 MHz specification plus a 25% margin). Here, $R_{\text{dyn}} \equiv dV/dI$ is the dynamic resistance of the components in the SQ1-bias loop (SQ1, R_{ser} , R_{b1} ; see Figs. 7 and 8), while L_{tot} is the series inductance in the SQ1-bias loop (dominated by the self-inductance of the SSA input coil and the wiring that connects the TES/SQ1 stage to the SSA stage). In X-IFU, it is desired to allow $L_{\text{wiring}} \leq 350$ nH, which is higher than in the 8×32 TDM-snout systems. In early

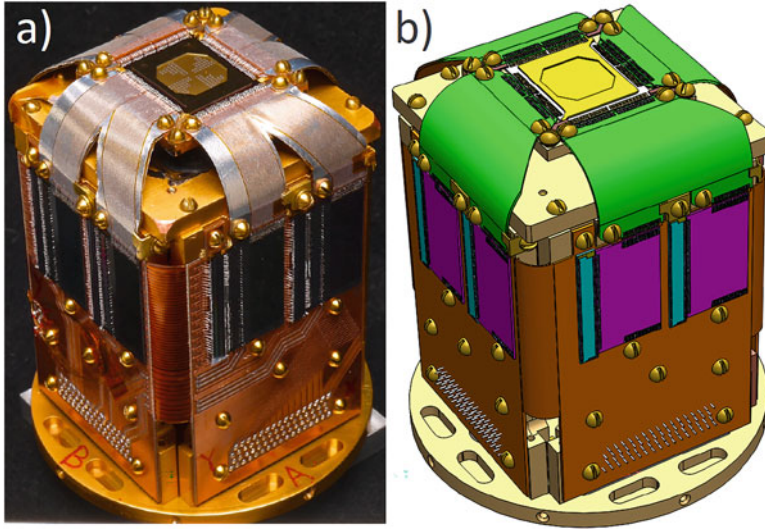


Fig. 9 The 50 mK snout package. (a) Photograph of the snout. The circular pedestal at the bottom of the image has a diameter of 58.4 mm and the snout has a height of 67 mm. (b) CAD image of the snout, with various parts highlighted in different colors. *Yellow*: The TES chip and X-ray aperture sit on top. *Green*: On flexible circuits, a total of 512 Al traces (256 pairs) run from the detector plane to the four side panels. *Purple*: The “interface chips” contain the TES-shunt resistors and the Nyquist inductors; there is one of these chips per TDM column, or eight chips in total. *Cyan*: The TDM multiplexer chips contain the SQ1s and FASs. *Orange*: A rigid-flexible printed circuit board (PCB) connects to the interface and TDM chips via Al wirebonds and wraps around the snout to carry signal lines from panel to panel. A trio of 65-lead “Nano-D” connectors on the inside of the rigid-flex PCB connect to twisted-pair cables that carry signals to and from higher-temperature cryogenic circuitry. (From Doriese et al. 2017; re-printed with permission)

2022, $R_{\text{dyn}} \geq 35 \Omega$ was demonstrated (Durkin et al. (2021) give an intermediate report of progress toward this milestone).

The second set of optimizations was to the packaging of the TDM componentry. Cryogenic components, such as the TES-shunt resistors (Doriese et al. 2019) and SQ1s, were shrunk in area. The various wire coils (SQ1-input transformer and Nyquist inductors) were designed in “even” and “odd” versions to allow close-packing of TDM cells in a two-dimensional grid without an increase in cell-to-cell inductive crosstalk. Most importantly, a cold-indium bump-bonding process (Lucas et al. 2022) was developed to allow attachment of the X-IFU TDM chips to the FPA side panels without the need for a challenging number of wirebonds.

The third optimization was a change in the architecture of the flux-actuated switches. X-IFU has baselined a “two-level-switching” scheme in which each TDM pixel retains its own “pixel-select” switch and a second layer of switch, a “cluster-select” switch, shorts out a larger cluster of pixels. This scheme’s chief advantage is a significant reduction in the number of wires needed for row addressing. Dawson et al. (2019) describe the idea further and provide some preliminary demonstrations.

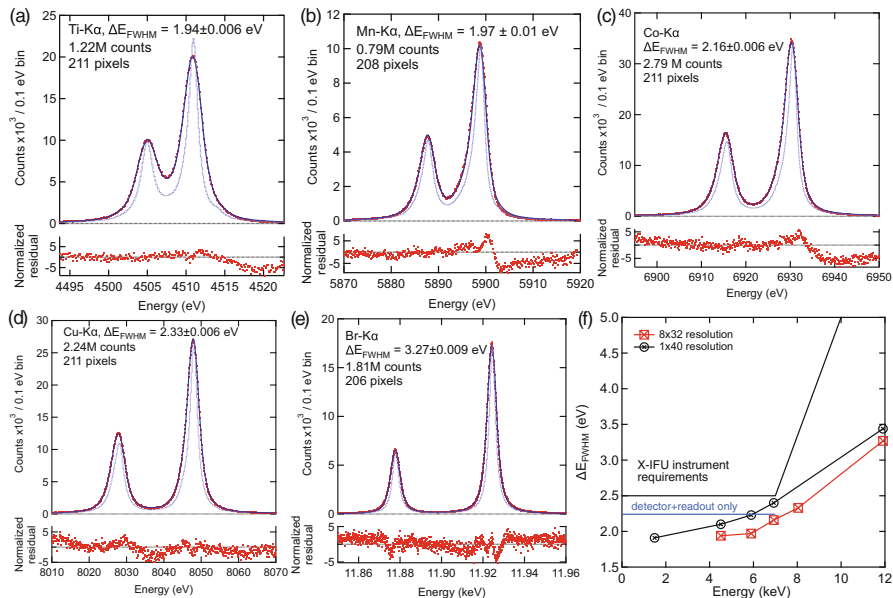


Fig. 10 Co-added 8-column by 32-row TDM spectra for (a) Ti- $K\alpha$, (b) Mn- $K\alpha$, (c) Co- $K\alpha$, (d) Cu- $K\alpha$, and (e) Br- $K\alpha$; all are measured from pure-metal foils except Br- $K\alpha$, which is measured from a KBr salt. The red dots in the main plots are the histogrammed spectra data, the light blue lines are the natural line shapes (not broadened by the finite resolution of the spectrometer), and the dark blue line is the best fit to the data. Below each main plot, the red dots show residuals (data minus fit). (f) ΔE_{FWHM} vs. X-ray energy for these 2019 measurements (red squares) and a previous data set acquired with a less mature version of the SQLs (black circles). The black line shows the X-IFU instrument-level requirements on energy resolution, while the blue line shows the requirements considering only the detector and readout subsystem and excluding margin. (From Smith et al., *IEEE Trans. Appl. Supercond.* (2021); re-printed with permission)

MHz Frequency-Domain Multiplexing (FDM)

In the MHz-FDM scheme, signals from the TESs are multiplexed in frequency space and the TESs are biased with megahertz-frequency alternating currents (ac bias) (Yoon et al. 2001; Cunningham et al. 2002; Kiviranta et al. 2002; Ullom et al. 2003; Dobbs et al. 2008; Takei et al. 2009). Each TES is connected to a passive LC resonator. The resonators are sufficiently separated in frequency space to avoid interferences (e.g., Fig. 11). Signals from the different TESs are summed in the front-end SQUID amplifier. There are three major advantages of the MHz-FDM architecture. First, the cold electronics are relatively simple (there is one DC-SQUID front-end amplifier per multiplexer chain). Second, MHz-FDM is relatively robust to electromagnetic interference (EMI) because the signals are transported at frequencies well above the electromagnetic disturbances due to the cryocoolers and the frequency dependence of the skin depth makes shielding easier and lighter. Third, MHz-FDM has lower environmental susceptibility (Vaccaro et al.

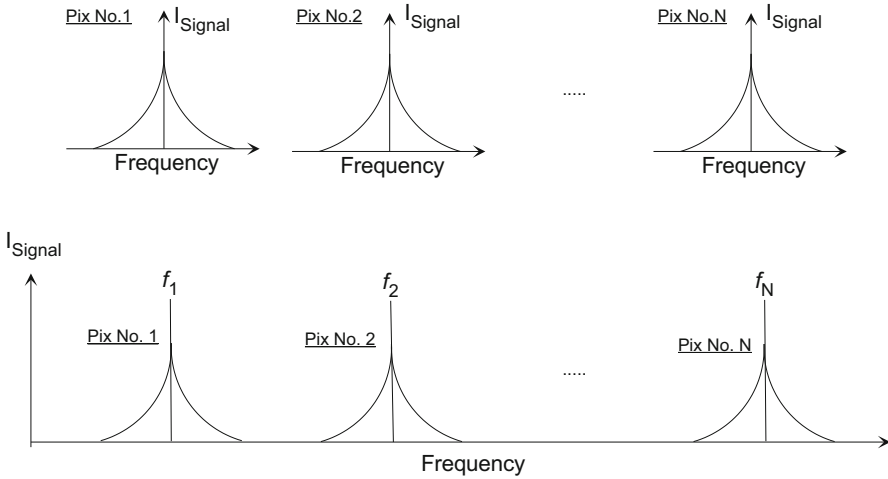


Fig. 11 Cartoon of the distribution of signals in frequency space in FDM. (top panel) In the TDM and μ mux readout schemes, the TESs are biased via a dc current so the signals are distributed around zero frequency. (bottom panel) In the FDM scheme, each TES is biased by its own MHz ac current and therefore the signals are distributed in frequency space. The bias frequencies of the TESs should be separated enough to avoid crosstalk between TESs. The signals are demodulated by the room-temperature electronics

2022b) (see also Gottardi and Smith in this book). The X-IFU demonstration model (Section “[Demonstration Model of Focal Plane Assembly of Athena X-IFU](#)”), on which we base this presentation of MHz-FDM, will use a second-stage series-array SQUID (Kiviranta et al. 2021) located on the 2 K stage. Multiplexed signals are demodulated per TES (per assigned frequency) in the room-temperature electronics.

The sum of signals can be achieved in several ways in SQUID readout: current summing (Kiviranta et al. 2004), flux summing (Mitsuda et al. 1999; Kimura et al. 2008), and voltage summing (Yoon et al. 2001; Cunningham et al. 2002). Traditionally, voltage summing has been performed via summing loops; however, because SQUIDs are inherently sensitive to changes in magnetic flux, and current is straightforwardly transduced to flux via a wire coil, it is more straightforward to sum the signals via current or magnetic flux. The flux-summing approach requires a separate input coil for each TES. This complicates the design of the SQUID and may cause electrical crosstalk between input coils via mutual inductance. On the other hand, the current-summing method does not require a complicated SQUID design, and crosstalk can be avoided via careful implementation of the coils. This section focuses mainly on the current-summing method.

The multiplexed signal is demodulated (at the assigned frequency) for each TES in the room-temperature electronics. The modulation (bias) frequency must be much higher than the signal bandwidth of the TES response (~ 50 kHz). Therefore, a readout bandwidth of several megahertz is necessary to ensure a reasonable multiplexing factor. As mentioned in the previous section, DC-SQUID

amplifiers combine sufficient bandwidth (~ 10 MHz) with a high flux dynamic range ($\sim 10^8$ or $\sim 0.01\mu\Phi_0/\sqrt{\text{Hz}}$). This allows multiplexing of tens of TES X-ray microcalorimeter signals, or more than 100 lower-bandwidth bolometric TESs, in a single readout chain.

In the FDM method, the signal-to-noise ratio is not degraded by an increased multiplexing factor as it is in the TDM method (see Eq. 6 in Section “[Circuit Parameters, Multiplexing Factor, and Noise Scaling](#)”). However, in FDM each TES must be activated by a megahertz-frequency ac bias, which introduces additional physical phenomena into the TES, such as the ac Josephson effect due to the lateral proximity effect of the superconducting leads (Sadleir et al. 2010, 2011; Gottardi et al. 2014a, 2018) (see also the chapter by Gottardi and Smith in this book for details). Sections “[Room-Temperature Electronics](#)” and “[Lithographic LC Filter](#)” detail some important technologies needed to realize FDM readout, while Sections “[Demonstrations](#)” and “[Demonstration Model of Focal Plane Assembly of Athena X-IFU](#)” describe some experimental demonstrations of FDM readout of X-ray-TES arrays.

Room-Temperature Electronics

The FDM room-temperature electronics consist of two main components: the analog electronics (Front-End Electronics, or FEE) and the digital electronics (DEMUX board).

FEE: The primary role of the FEE is to amplify the signal from the cryogenic SQUID array so its signal size and output-voltage noise are compatible with the room-temperature ADC. A low-noise amplifier (LNA) is thus needed. The FEE developed at SRON, pictured in Fig. 12, has an input-voltage noise of ~ 300 pV/ $\sqrt{\text{Hz}}$. Information about the SRON FEE can be found in the literature (Wang et al. 2020).

DEMUX board: The DEMUX board handles many functions, including demodulation of signals and generation of the TESs’ ac-bias carrier combs and the feedback signal applied to the front-end SQUID. In addition, the DEMUX board

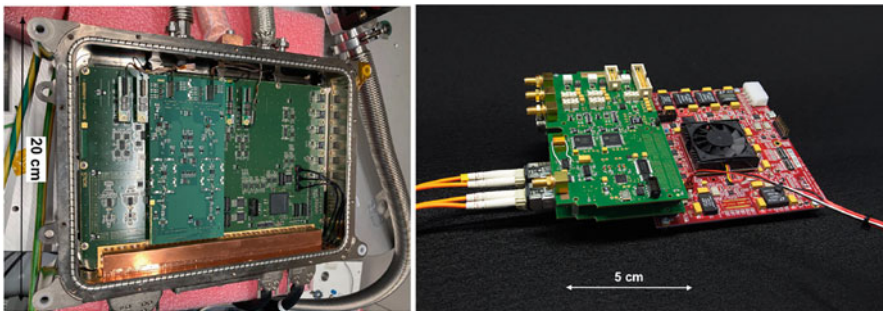


Fig. 12 *Left:* photograph of the dual FEE with two-channel LNA and SQUID controller. *Right:* photograph of the DEMUX board for FDM readout. Both of these electronics were developed at SRON

must be capable of handling delays and phase shifts introduced by the environment. In the presence of the long wiring harnesses that are expected in satellites, (For Athena X-IFU instrument, the length of the harness between the 50 mK stage and the room-temperature digital electronics may be as long as 5 m. For other similar cryogenic instruments such as SPICA/SAFARI (Roelfsema et al. 2012), even longer harnesses (~ 12 m) have been proposed.) standard feedback methods (e.g., the conventional flux-locked loop, or FLL) do not properly compensate the input signal to the SQUID's amplifier due to the phase difference between the input signal and the feedback signal. The lack of phase margin in a standard FLL would thus make the feedback loop unstable above some maximum frequency, f_{\max} . The gain-bandwidth product, $f_{\max} * G_{\text{FB}}$, of a standard FLL controller is limited by the phase shift due to signal travel time through a total travel length in the cable, l , as (den Hartog et al. 2009):

$$f_{\max} * G_{\text{FB}} = \frac{c}{8l\sqrt{\eta}}, \quad (7)$$

where G_{FB} , c , and η are the loop gain of the feedback, the speed of light, and the dielectric constant of the cable's dielectric material, respectively. Assuming $G_{\text{FB}} = 10$ (which is required to keep the total flux in the linear regime of SQUID response) and $\eta=3$, for a 1 m cable harness ($l = 2$ m for the round-trip travel distance of signal and feedback), the maximum frequency will be about 1 MHz. With even longer cables and FDM's higher bias frequencies, standard FLLs cannot work.

Baseband feedback (BBFB den Hartog et al. 2009; Fig. 13) is one way to overcome this limitation (Another method is digital-active nulling (DAN de Haan et al. 2012). The main difference is that in BBFB there is feedback to the summing junction shared by the carrier voltage. DAN is or will be implemented in the SPT-3G instrument (Montgomery et al. 2022) and the LiteBird satellite (Hazumi et al. 2020; de Haan et al. 2020)). The BBFB method sends the signal from the TES back to the SQUID after correcting for delay and phase rotation at each carrier frequency. BBFB significantly improves the bandwidth, linearity, and dynamic range of the SQUID amplifier. At SRON, the DEMUX board consists of an AD9726 16-bit DAC and a Xilinx XC7V585T Virtex 7 field-programmable gate array (FPGA). Signals are measured at 20 MSample/s and decimated to 156.3 kSample/s by a four-stage filter. The DAC performance is described by den Hartog et al. (2018). The firmware of the DEMUX board will allow up to 64 X-ray microcalorimeters or up to 172 bolometers (Fig. 14).

Lithographic LC Filter

High-quality LC resonators/filters are one of the key cryogenic components to achieve high multiplexing factors in FDM readout; a higher density of LC filters allows more efficient use of the available bandwidth. However, there is a trade-off between fabrication accuracy due to technology limitations and performance metrics such as crosstalk and stability. For a single-pole LC filter, the resonator bandwidth

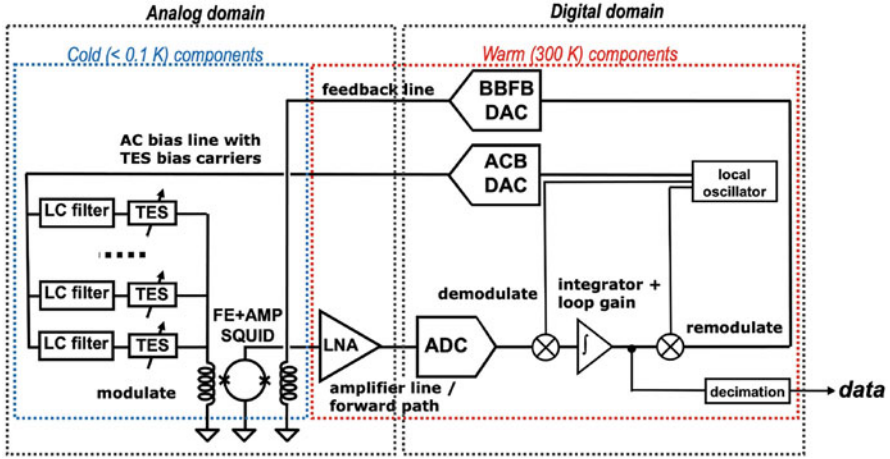


Fig. 13 Block diagram of the FDM readout architecture. The ac-bias carrier is generated in the FPGA and converted to an analog signal by a DAC in the digital electronics (DEMUX board). Each TES in the readout channel is equipped with an LC filter with a unique frequency; the two-stage SQUID is read out by an LNA (low-noise amplifier) at room temperature. Signals are converted from analog to digital by an ADC and demodulated by an FPGA. The demodulated signal is decimated by a four-stage filter to reduce the data volume. The final sampling rate is 156.3 kSample/s. The feedback signal is calculated and fed back to the system after compensating for phase delays caused by electronics and the length of the wiring harness in the system. (From den Hartog et al. 2009; re-printed with permission)

(Δf_{BW}), resonant frequency (f_c), and quality (Q) factor are described as follows:

$$\Delta f_{BW} = \frac{R}{2\pi L}, \quad f_c = \frac{1}{2\pi\sqrt{LC}}, \quad \text{and} \quad Q = \frac{1}{R}\sqrt{\frac{L}{C}}, \quad (8)$$

where R and L represent the total resistance and inductance, respectively. Typically, the same inductance value is used for different LC filters and the resonant frequencies are tuned via the capacitance. In this way, the design and uniformity of the LC filter can be well controlled. It is common for proposed satellite-borne FDM systems to have a minimum bias frequency of about 1 MHz. This is because at lower frequencies, the area required for the capacitors begins to dominate the overall area of the cryogenic components. At the higher-frequency end of the readout band, challenges arise due to the equivalent series resistance (ESR) generated in the dielectric medium within the capacitor, the analog bandwidth in the full chain, and power dissipation in the warm electronics.

SRON uses an LC filter with a $2\ \mu\text{H}$ coil. A superconducting transformer is also used to adjust the detector bandwidth via the damping inductance. SRON's LC filter is fabricated via lithographic technology (Bruijn et al. 2014, 2018).

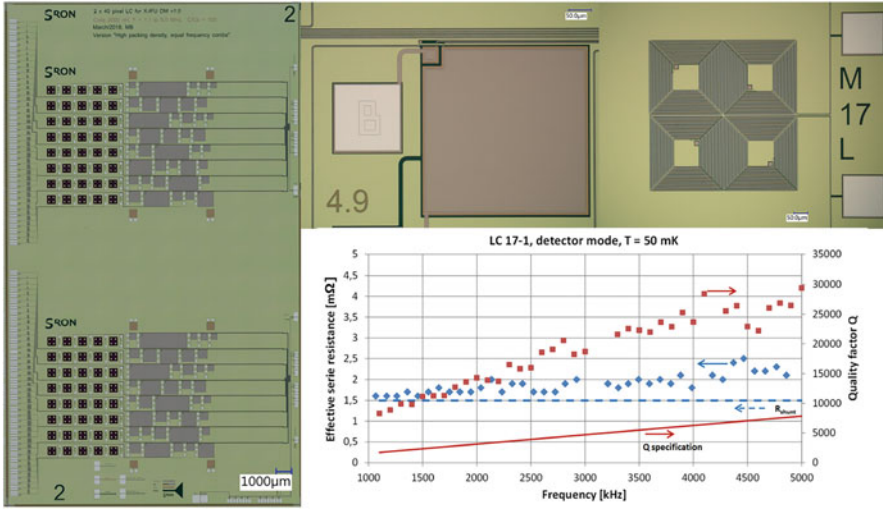


Fig. 14 *Left*: photograph of a lithographic LC filter chip containing 2×40 resonators. The chip size is $36 \text{ mm} \times 60 \text{ mm}^2$. *Upper right*: an enlarged photograph of one capacitor (left) and one $2 \mu\text{H}$ spiral coil with back-spiraling return line (right). *Bottom right*: effective series resistance (blue diamonds) and quality factor (red squares) of the LC resonators vs. frequency (Bruijn et al. 2014, 2018). The blue-dashed and red-solid lines indicate the contribution of the shunt resistance and the Q specification of this design

Demonstrations

Achievement of the best energy resolution in TES X-ray microcalorimeters under FDM readout has required resolution of several deep and difficult issues related to the fundamental physics of superconductivity and SQUID readout (Akamatsu et al. 2020). The three main areas of research over the last 10+ years have been (1) the physics of superconducting thin films under ac bias (Sadleir et al. 2010, 2011; Akamatsu et al. 2014; Gottardi et al. 2014b, 2018), (2) performance degradation due to carrier leakage (van der Kuur et al. 2004; Akamatsu et al. 2020), and (3) performance degradation due to intermodulation products (van der Kuur et al. 2016; Vaccaro et al. 2021; van der Hulst et al. 2021). As of late 2021, all issues were resolved; Akamatsu et al. (2021) give more information on these issues and their resolution.

Figure 15 (upper) shows a two-column FDM demonstrator developed at SRON. It employs magnetic shields of both high- μ and superconducting (Nb) materials against the earth's magnetic field (Bergen et al. 2016). The system is installed in a dry dilution refrigerator with a vibration-reduction mechanism (Gottardi et al. 2019). Forty LC resonators, each consisting of a $2 \mu\text{H}$ coil (Bruijn et al. 2014, 2018), a capacitor, and a superconducting transformer, were implemented to tune the electrical circuits seen by selected TESs in a kilopixel array of SRON X-ray TESs (Nagayoshi et al. 2020; Taralli et al. 2020; D'Andrea et al. 2021). The effective inductance seen by the TES (equivalent to L_{N_y} in TDM) is tuned to be 60% of the critical inductance at a TES resistance of 15% of R_n . The resonator centers span

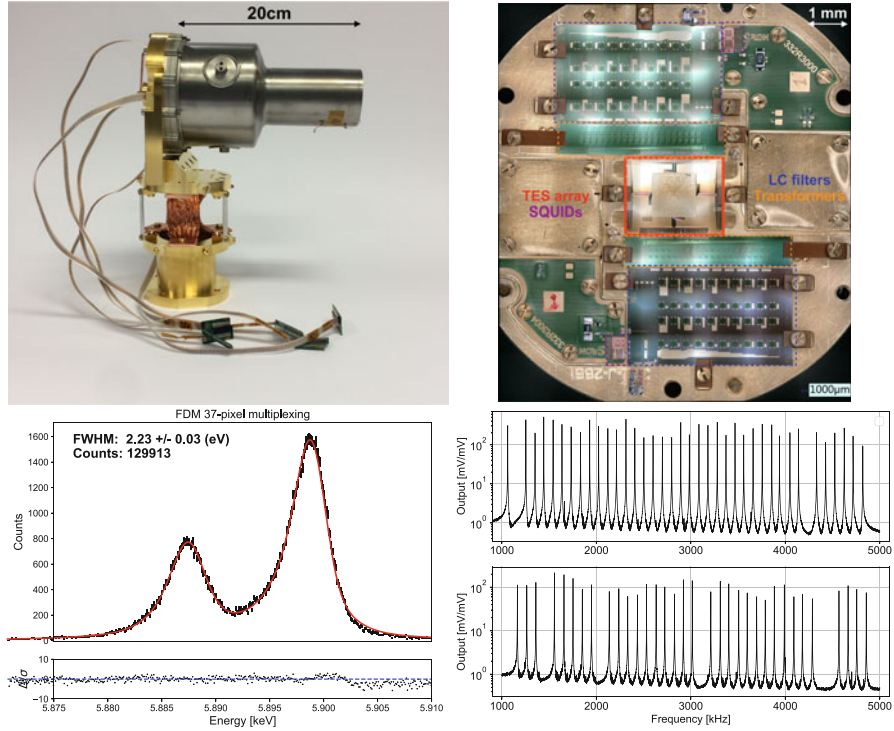


Fig. 15 *Upper left*: photograph of the two-column FDM-readout demonstrator. The gray cylinder is the Nb superconducting magnetic shield. *Upper right*: photograph of the focal plane showing the SRON kilopixel TES array (Nagayoshi et al. 2020), superconducting transformers, LC filters, and FE SQUIDs. Two FDM columns are connected. *Lower left*: co-added energy spectrum of the Mn-K α complex from 37 TES pixels under FDM readout with a combined energy resolution of 2.2 eV at 6 keV (Akamatsu et al. 2021). The spectral data were fitted to the Mn-K α line model of Hölzer et al. (1997) convolved with the Gaussian detector response. Cash statistics (Cash 1979; Kaastra and Bleeker 2016) are employed to avoid fitting bias. *Lower right*: resonator distribution vs. frequency for column 1 (top) and column 2 (bottom) of the two-column FDM system

the 1 to 5 MHz readout bandwidth with 100 kHz separation, meaning there are 40 resonators per column. The rms scatter of the frequency centers is about 4 kHz and is dominated by lithographic accuracy. A two-stage SQUID is employed, which is provided by VTT/Finland (Kiviranta et al. 2018, 2021). Figure 15 (lower left) shows a co-added X-ray spectrum of the Mn-K α complex from 37 multiplexed pixels (two resonators did not yield and one pixel was turned off); the achieved energy resolution was $\Delta E_{\text{FWHM}} = 2.23$ eV at 6 keV. In a different experiment performed in a different cryo-module (Akamatsu et al. 2014), 31 multiplexed TESs achieved a summed spectral resolution of $\Delta E_{\text{FWHM}} = 2.14$ eV. The level of the thermal crosstalk is evaluated to be $\sim 10^{-4}$ (Vaccaro et al. 2022c) for pixels that are physically nearest neighbors, which surpasses the Athena X-IFU instrument requirement of $< 10^{-3}$.

The performance degradation due to readout is estimated to be 0.9 eV in quadrature (see Fig. 3 in Akamatsu et al. 2021) and is dominated by known and non-fundamental problems such as thermal gradients in the cryogenic stage. In other words, there is ample room for further improvement and increasing multiplexing factor in future experiments. A two-column FDM demonstration is currently underway (see Fig. 15 bottom right).

Demonstration Model of Focal Plane Assembly of Athena X-IFU

An important application of FDM readout of TES X-ray microcalorimeters is verification of the demonstration model (DM) of the Athena X-IFU focal plane assembly (FPA (Jackson et al. 2016); see Fig. 16). The X-IFU FPA DM is designed to investigate various technological challenges. The X-IFU FPA DM hosts a kilopixel TES array that was extensively characterized under ac bias (Taralli et al. 2020; Taralli et al. 2021; D'Andrea et al. 2021), an anticoincidence detector (Macculi et al. 2016; D'Andrea et al. 2017, 2020), and four FDM columns with 20 pixels per column connected (i.e., 80 TESs in total). The X-IFU FPA DM has three main purposes:

1. A test bed for key technology items that have not yet been demonstrated at all, or have not been demonstrated in combination with other parts of the FPA. Examples are the dual-stage SQUID amplifiers which are divided over two temperature stages, the magnetic shields, and the Kevlar suspension (see Fig. 16 top left). (Micro-vibration can degrade the performance of the instrument significantly. It is of importance to isolate the instrument from the source of the vibration. See Takei et al. (2018) for more details of a similar investigation for Hitomi/SXS.)
2. A physical reference for thermal, magnetic, and mechanical simulations that will guide the design of the engineering model and eventually the flight model. Measurements obtained from the FPA DM allow the simulations to be checked and, when necessary, can guide improvements to the simulations.
3. A demonstrator for the environments in which the TES sensor array needs to perform. As the main task of the FPA is to shield the TES array from adverse thermal, magnetic, and mechanical influences from outside, the FPA DM will provide a test in the environment of a cryostat. In particular, it will serve as a demonstrator of the 2K core in the CEA Cryostat XIII, where the FPA will be operated in proximity to an adiabatic demagnetization refrigerator and flight-representative Joule-Thomson coolers.

As of August 2022, the following milestones had been met:

1. the thermal loads on the various cryogenic stages were measured;
2. temperature stability of the detector stage was $0.9 \mu\text{K}$ with 1 s sampling repetition over the required period of more than 1 hour; and
3. on the first cool-down of the system, energy resolution better than 2.5 eV at 6 keV was demonstrated.

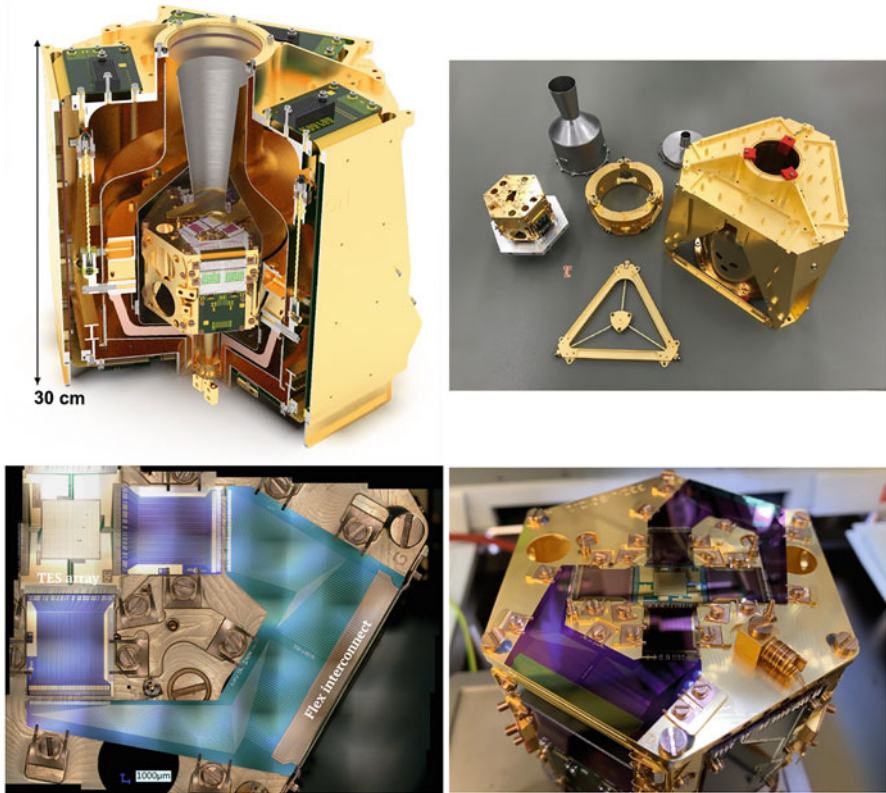


Fig. 16 *Top left:* CAD-rendered image of the X-IFU FPA DM. Inside the gold-plated copper housing are two magnetic shields (high- μ metal and superconducting Nb) and a prototype of the 50 mK detector assembly. The FPA is suspended by Kevlar wires to damp micro-vibrations from the mechanical cryocoolers and to thermally isolate the 50 mK stage from the 2 K environment. *Top right:* photograph of some disassembled components of the X-IFU FPA DM. The triangular component is the mechanical supporting structure based on Kevlar wires. *Bottom left:* photograph of the flexible-interconnect chip (van Weers 2013). *Bottom right:* photograph of the 50 mK detector assembly. The central kilopixel TES array is connected to four FDM columns with 20 pixels per column

These results verify that the thermal and mechanical environment provided by the FPA is suitable for the needed performance in X-IFU.

Microwave-SQUID Multiplexing (μ mux)

Multiplexing techniques utilizing gigahertz of bandwidth became possible with the development of low-thermal-conductance cryogenic microwave cables, in the form of narrow gauge Cu-Ni and Nb-Ti coaxial cables, and a low-noise cryogenic

microwave amplifier, in the form of the high-electron-mobility transistor (HEMT) amplifier (Duh et al. 1988) (Fig. 17).

Microwave-SQUID multiplexing (μ mux) (Mates et al. 2008, 2017; Hirayama et al. 2013; Ahrens et al. 2019) is a form of frequency-domain multiplexing that allocates this bandwidth between input channels by the use of distinct, high- Q microwave resonances, each coupled to its own rf-SQUID and reading out the current signal from its own detector. As a superposition of microwave tones passes through the circuit, each tone is modulated by its own SQUID/resonator circuit before being amplified by the HEMT and brought to room temperature on a single coaxial cable (Fig. 18).

An example circuit is shown in Fig. 19. In this circuit, distributed quarter-wave resonators of different lengths are capacitively coupled to a common microwave “feedline” at one end and inductively coupled to their individual SQUIDs at the other end. Two notable variations utilize lumped-element resonators (Ahrens et al. 2019) rather than quarter-wave resonators and direct incorporation of the SQUID

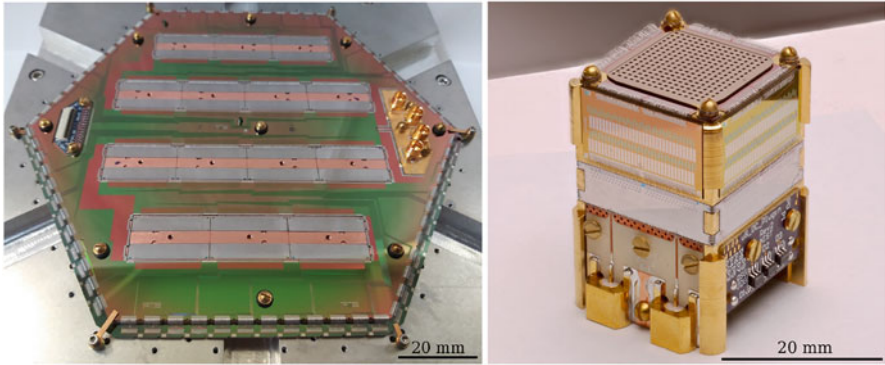


Fig. 17 *Left* μ mux readout circuitry on the backside of a 1,820 pixel CMB polarimeter array, read out by 28 μ mux chips on two pairs of coaxial cables. *Right* “microsnout” readout package for 256 X-ray microcalorimeters. The microsnout is modular: microsnouts can be tiled within a focal plane and electrically connected in series within a multiplexer channel

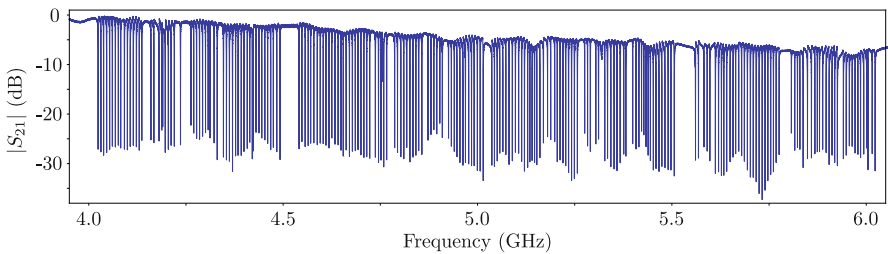


Fig. 18 Survey of microwave transmission $|S_{21}|$ through a microwave-SQUID multiplexer operating in the 4 to 6 GHz band, with 256 channels distributed across four discrete μ mux chips

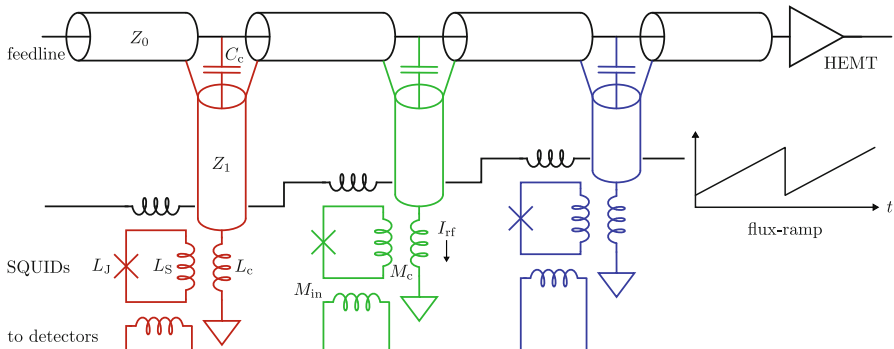


Fig. 19 Schematic of a three-pixel microwave-SQUID multiplexer, consisting of quarter-wave resonators inductively coupled to rf-SQUIDs. Resonance frequencies are set by the lengths of the transmission lines, resonance bandwidths by C_c , and resonance frequency shifts by M_c , L_S , and L_J

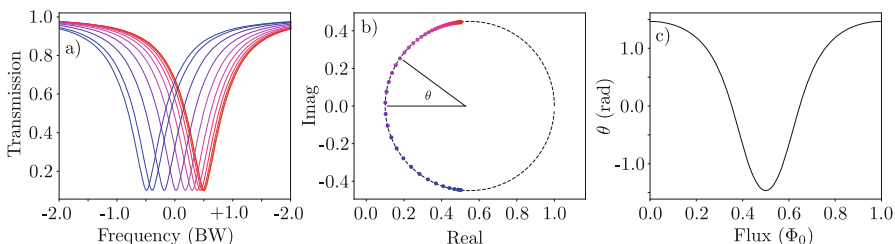


Fig. 20 Illustration of the principle of operation of a microwave-SQUID multiplexer channel. (a) The resonance frequency shifts in response to magnetic flux. (b) For a fixed microwave frequency, the complex transmission parameter S_{21} describes an arc on a circle. (c) The SQUID response is periodic with a magnetic flux quantum Φ_0

into the resonator (Hirayama et al. 2013) rather than inductive coupling to the SQUID.

In any implementation, the multiplexer works by loading the resonator with the flux-variable inductance of a Josephson junction:

$$L_J(\phi) = \frac{\Phi_0}{2\pi I_c \cos(\phi)} \quad (9)$$

where I_c is the critical current of the Josephson junction, Φ_0 is the magnetic flux quantum, and $\phi \equiv 2\pi(\Phi/\Phi_0)$ is the difference in phase of the superconducting wave function across the junction.

As the flux in the rf-SQUID varies, the inductive load it applies to the resonator varies, both positively and negatively, causing the resonance frequency f_0 to change without significant change in microwave loss (Fig. 20). For a fixed microwave probe

Table 3 Table of equations describing the behavior of a SQUID-resonator pair. Most variables are defined in Fig. 19. Φ_{rf} is the amplitude of microwave flux excitation in the SQUID, ΔL_{pp} is the peak-to-peak variation in load inductance with flux, Δf_{BW} is the resonator bandwidth, and P_{feed} is the power per tone on the feedline. For a lumped-element design, L and C are the lumped inductance and capacitance of the resonator, respectively

SQUID coupling:	Inductive	Direct
Φ_{rf}	$M_c I_{\text{rf}}$	$L_S I_{\text{rf}}$
ΔL_{pp}	$\frac{2M_c^2}{L_J(1-\lambda^2)}$	$\frac{2\lambda^2 L_J}{1-\lambda^2}$
Resonator type:	Quarter-wave	Lumped-element
$\frac{df_0}{dL}$	$-\frac{4f_0^2}{Z_1}$	$-\frac{\pi}{\sqrt{L/(C+C_c)}}$
Δf_{BW}	$8\pi f_0^3 C_c^2 Z_0 Z_1$	$2\pi^2 f_0^3 C_c^2 Z_0 \sqrt{L/(C+C_c)}$
P_{feed}	$\frac{\pi Z_1 \Delta f_{\text{BW}}}{16f_0} I_{\text{rf}}^2$	$\frac{\Delta f_{\text{BW}}}{4f_0} \sqrt{L/(C+C_c)}$

tone, the complex transmission traverses an arc on a circle with the angular position on this arc being a periodic function of magnetic flux.

One key parameter of the rf-SQUIDs is the ‘‘screening parameter’’ λ (Likharev 2022), sometimes denoted β_L , which gives the ratio of SQUID self-inductance to Josephson inductance:

$$\lambda \equiv \frac{L_S}{L_J} = \frac{2\pi I_c L_S}{\Phi_0}. \quad (10)$$

For $\lambda < 1$, the SQUID response is single-valued, while for $\lambda > 1$, the SQUID may switch hysteretically between multiple states (Likharev 2022). An rf-SQUID may be operated in the hysteretic regime, but it requires damping to make its behavior predictable. Because this damping would limit resonator Q -factors, microwave-SQUID multiplexers operate in the non-hysteretic regime, typically targeting $\lambda \approx 1/3$.

Table 3 lays out some of the equations (Mates 2011) describing the behavior of an rf-SQUID and resonator pair. Although these equations are only strictly valid in the regime of low-power slow flux-ramp, they provide a useful guide to device design.

For example, the equations show how M_c and C_c may be adjusted in tandem to achieve designs with different pixel bandwidths while holding the ratio of peak-to-peak frequency shift to bandwidth ($\eta \equiv \Delta f_{\text{pp}}/\Delta f_{\text{BW}}$) constant. They further show that the microwave-flux excitation (on-resonance and in the inductive coupling, quarter-wave-resonator configuration of Fig. 19) in the SQUID is related to the power-per-tone on the feedline as:

$$P_{\text{feed}} = \Phi_{\text{rf}}^2 \frac{\pi^2 f_0 I_c}{\eta \Phi_0 (1 - \lambda^2)}. \quad (11)$$

In Section “[μmux Readout Noise](#)” we will use this information to derive expected readout noise and discuss the trade-off between noise and maximum signal slew rate. In Section “[μmux Crosstalk](#)” we will discuss the trade-off between frequency packing and crosstalk. This analysis will show what capabilities we can expect of a μmux system designed for any particular application.

Flux-Ramp Modulation

With microwave-SQUID multiplexing, there is no practical way to apply feedback without the addition of a large number of wires. Instead, a flux-ramp modulation scheme (Mates et al. 2012) is typically employed that sweeps rapidly across the SQUID response such that the input signal is transduced into a phase shift of the response function (Fig. 21). This phase may then be extracted at room temperature either with a fit or with Fourier techniques over an integral number of oscillations. The initial section of the flux-ramp response is usually contaminated with a transient from the reset and must be discarded, with analysis only over a useful fraction α .

This both linearizes the SQUID readout and upconverts it above the significant low-frequency noise that is due to two-level systems, while reducing the readout signal power by approximately $\frac{\alpha}{2}$, where the factor of $\frac{1}{2}$ arises from averaging across the roughly sinusoidal SQUID response curve and the factor of α arises from discarding transient-contaminated data.

The flux-ramp repetition rate f_r thus becomes the sampling rate of the input signal. To fit the SQUID modulation within the resonator bandwidth, it must obey $f_r n \Phi_0 < \Delta f_{BW}/2$, where $n \Phi_0$ is the number of flux quanta per ramp. It must also substantially exceed the frequency content of the input signals in order to read them out accurately, as the fidelity of the modulation scheme begins to degrade at an input signal slew rate of order $f_r \Phi_0/2$. These considerations determine the resonator bandwidth necessary for readout of a detector system.

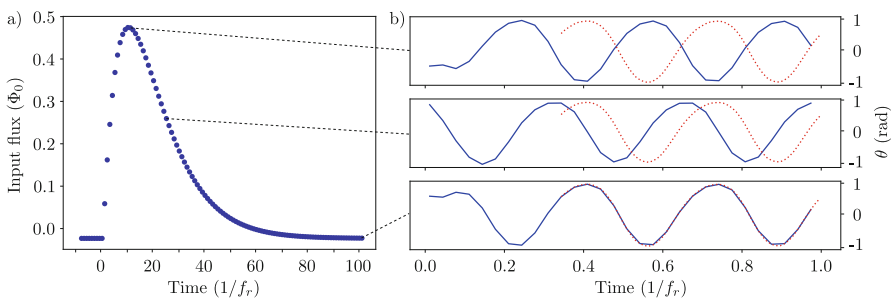


Fig. 21 Illustration of the principle of flux-ramp modulation, which transforms (a) the input flux signal into (b) a phase shift of the SQUID response, shown as blue lines with the baseline response as dashed-red lines. The flux-ramp reset transient is visible at the start of each ramp response window

μ mux Readout Noise

There are multiple sources of noise in a microwave-SQUID multiplexer: HEMT-amplifier noise is generally dominant, two-level system noise becomes significant for narrow resonator bandwidths, and digital noise limits the number of tones we can cleanly generate and digitize in a set of room-temperature electronics.

The HEMT amplifier produces broadband white noise with typical noise temperatures on the order of $T_N \approx 4$ K ($k_B T_N \approx -193$ dBm/Hz). To convert this noise to units of magnetic flux, we must find the power in the microwave probe tone, which should be as large as possible, up to the limits of SQUID nonlinearity.

Determination of the optimal value of P_{feed} requires analysis beyond the linear, small-signal approximations of the equations in Table 3, including nonlinear and nonequilibrium dynamics. As Φ_{rf} grows to a significant fraction of Φ_0 , the SQUID inductance stops being effectively constant over the microwave excitation and siphons power from the microwave-probe frequency into higher harmonics. This behavior can be analyzed in expansion (Wegner et al. 2022), but to include all complicating phenomena generally requires simulation.

Figure 22 shows the results of simulations that include different sets of complicating factors, and in which we find the optimal microwave flux amplitude to be $0.25 \Phi_0$ to $0.4 \Phi_0$, depending on design parameters. For an example set of design parameters ($\eta = 1$, $f_0 = 6$ GHz, $I_c = 5 \mu\text{A}$, $\lambda = 1/3$), this yields a tone power on the feedline of -73 to -70 dBm, or approximately 120 dB above the 1 Hz noise power of the HEMT, and an arc of approximately ± 1 radians.

This gives a noise spectrum in θ , the angle on the resonance arc (Fig. 20) of:

$$S_\theta = \left(\frac{1 - Q/Q_i}{2} \right)^{-2} \frac{k_B T_N}{P_{\text{feed}}} \approx 4 \frac{k_B T_N}{P_{\text{feed}}} \quad (12)$$

where the first term gives the radius of the resonance circle in terms of the total quality factor Q and internal quality factor Q_i . The approximation assumes $Q_i \gg$

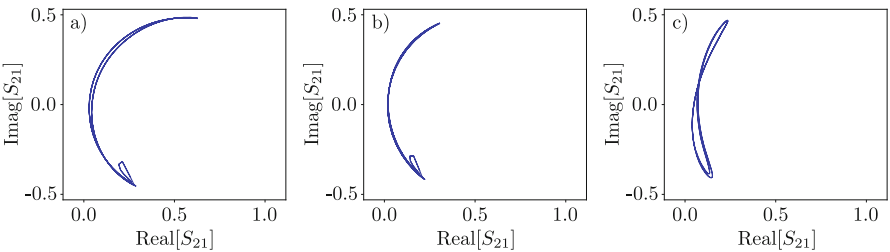


Fig. 22 Nonlinear, nonequilibrium simulation results showing various ways in which the SQUID response departs from the simple theory in practical operation. (a) Low-power, slow flux-ramp, but with a significant flux-ramp-reset transient. (b) Slow flux-ramp but with high microwave-drive power that suppresses the amplitude of the SQUID response. (c) High-power, fast flux-ramp so that the resonator never has time to fully equilibrate and instead follows a “figure-8” trajectory along the resonance circle

Q , but for narrow resonance applications (<100 kHz) Q_i may approach the total Q , which increases this noise contribution.

We can then assume a sinusoidal SQUID response, as shown in Fig. 21, with an amplitude of $\theta_{\max} \approx 1$ and apply the flux-ramp modulation penalty to get:

$$S_{\Phi}^{\text{HEMT}} = S_{\theta} \left(\frac{\Phi_0}{2\pi\theta_{\max}} \right)^2 \frac{2}{\alpha} \approx \frac{k_B T_N}{P_{\text{feed}}} \frac{4}{\pi^2} \Phi_0^2 \quad (13)$$

where in the final approximation we have assumed a $2\Phi_0$ flux ramp and have discarded the first oscillation for $\alpha = \frac{1}{2}$. This implies a HEMT contribution to readout noise of approximately $0.7 \mu\Phi_0/\sqrt{\text{Hz}}$. Although this theoretical limit is rarely achieved, total readout noise of $(1.0 \text{ to } 2.0) \mu\Phi_0/\sqrt{\text{Hz}}$ is common and sufficient for most low-temperature detector applications (see chapter by Gottardi and Smith in this book).

Two-level-system (TLS) noise arises from the coupling of the microwave fields in the resonator to two-level systems in the dielectrics. This produces a fractional-frequency noise that depends on temperature, internal power, material, and geometry (Gao et al. 2008). The power spectrum of this noise has a characteristic $1/\sqrt{f}$ frequency dependence, which the flux-ramp modulation of Section “Flux-Ramp Modulation” helps to avoid.

The TLS noise is not stationary over the period of the SQUID response, but we may bound its contribution by considering the equivalent flux noise at the steepest slope of the SQUID response, where:

$$\frac{d\theta}{d\Phi} = \theta_{\max} \frac{2\pi}{\Phi_0} \quad \text{and} \quad \frac{d\theta}{df} = \frac{4}{\Delta f_{\text{BW}}} = 4Q/f_0 \quad (14)$$

so that (again assuming $\theta_{\max} \approx 1$) the implied contribution to flux noise is:

$$S_{\Phi}^{\text{TLS}} = \frac{S_{\delta f_0}}{f_0^2} \left(\frac{2Q}{\pi} \right)^2, \quad (15)$$

which scales with Q or inversely with the resonance bandwidth.

The number of factors determining the TLS noise makes it difficult to make a general statement about its level, but measured fractional-frequency noise for the geometry, materials, and internal power of a typical μmux device is less than $S_{f_0}/f_0^2 \approx 10^{-19} \text{ Hz}^{-1}$ at 1 kHz. For example, in a 2 MHz resonator at 6 GHz, modulated at 1 MHz, we therefore expect a TLS noise contribution of less than $0.1 \mu\Phi_0/\sqrt{\text{Hz}}$. For multiplexers optimized for typical X-ray applications, with 1 MHz to 10 MHz resonator bandwidths, this contribution tends to be substantially less than the contribution of the amplifier chain.

Finally, any system for synthesizing and digitizing a large number of microwave tones adds its own noise: digital-quantization noise, clipping noise, and a pseudo-white noise of intermodulation products due to the imperfect linearity of the DACs

and ADCs. This is usually described by a dynamic range between the tone powers and the digital-noise floor. A careful analysis of this noise (Bennett et al. 2014) is beyond the scope of this chapter, except to say that multiplexing factors of ~ 1000 push the limits of existing digitizers, which requires multiple digitizers to cover the full band with sufficient dynamic range, but that digitizer capabilities are advancing rapidly and can be expected to continue to both improve in capability and fall in cost.

μ mux Crosstalk

There are three main mechanisms of crosstalk in the microwave-SQUID multiplexer (Mates et al. 2019): Lorentzian-tail crosstalk, coupled-harmonic-oscillator crosstalk, and broadband-nonlinearity crosstalk. Each constrains the multiplexer design in a different way.

Lorentzian-tail crosstalk arises from the quadratic falloff of the Lorentzian resonance shape, which allows one resonance to affect the transmission of a probe tone at the frequency of a neighboring resonance. For inductive coupling:

$$\chi_{\text{Lorentz}} \approx \frac{|S_{21}|^2}{2} \left(\frac{\Delta f_{\text{BW}}}{f_2 - f_1} \right)^2 \quad (16)$$

where χ gives the fractional crosstalk between the flux-ramp-modulated signals.

This mechanism dictates the minimum-frequency spacing between resonances as a multiple of their bandwidths and therefore the ultimate bandwidth efficiency. For part-per-thousand crosstalk between frequency neighbors, a target frequency spacing of (7 to 10) Δf_{BW} is typically necessary.

Coupled-harmonic-oscillator crosstalk arises when resonances are both electromagnetically coupled and close in frequency, such that the Eigen modes of the system are actually linear combinations of the uncoupled-resonance modes:

$$\chi_{\text{CHO}} \approx \left(\frac{4\bar{f}^2}{f_2 - f_1} \frac{M_x}{Z_0} \right)^2 \quad (17)$$

where M_x is the mutual inductance between resonance terminations. Other mechanisms of electromagnetic coupling add similar terms.

This mechanism motivates a design feature seen in all multiplexers that utilize superconducting resonators, which is the placement of frequency-adjacent resonators far apart in physical space and of physically adjacent resonators far apart in frequency space (Noroozian et al. 2012).

Broadband-nonlinearity crosstalk occurs within the broadband microwave components, such as the HEMT amplifier and room-temperature mixers, whose slight nonlinearity allows a third-order mixing process to transfer a fraction χ_{nonlin} of the modulation sidebands of one carrier tone to another:

$$\chi_{\text{nonlin}} \approx 4 \frac{P_{\text{feed}} |S_{21}|^2}{P_{\text{IP3}}} \quad (18)$$

where P_{IP3} is the third-order intercept point (here, referred to the input of the HEMT), which is the standard measure of cubic nonlinearity in amplifiers and mixers.

While this crosstalk is typically less than that of the other mechanisms, it is all-into-all and therefore remains of serious design concern. To reduce this crosstalk, we must use broadband components with high P_{IP3} or reduce the microwave power per tone at the cost of readout noise.

μ mux Optimization for X-ray Applications

For each application, the following optimization should be performed:

1. Design the input coupling M_{in} such that the readout noise will not significantly degrade the detector signal.
2. Calculate the flux-ramp rate necessary to accommodate the signal slew rate, which determines the resonance bandwidth.
3. Space the resonance frequencies by a multiple of their bandwidths that is sufficient to meet the required crosstalk limits.

For a $2\Phi_0$ flux-ramp and $10 \Delta f_{BW}$ spacing for part-per-thousand crosstalk, this implies a multiplexing factor of:

$$N \approx \frac{\Delta f_{BW-tot}}{80} \frac{\Phi_0}{M_{in} \left| \frac{dI}{dt} \right|_{max}} \quad (19)$$

which is the number of detectors that can be read out using one HEMT, a pair of coaxial cables, and a flux-ramp line.

As an abstract example, a signal with a maximum slew rate of $0.05 \Phi_0/\mu s$ would require a flux-ramp rate of 100 kHz, a resonance bandwidth of 400 kHz, and achieve a multiplexing factor of $\sim 1,000$ in a 4 to 8 GHz HEMT. This is more than an order of magnitude higher than can be provided by conventional multiplexing technologies ($N \sim 40$ by TDM and FDM).

Traditional X-ray applications with relatively high count rates are generally well-matched to the practical range of μ mux designs. As the count rate falls substantially below ~ 100 Hz, it becomes difficult achieve the resonator bandwidth (to less than 100 kHz) and resonance frequency placement (to better than 1 MHz). Reliable μ mux designs have been proven for a range of bandwidths from 100 kHz to 30 MHz.

Example μ mux Systems

The first fielded application of μ mux readout for TES microcalorimetry was the SLEDGEHAMMER instrument at Los Alamos National Laboratory (Mates et al. 2017), in which 128 gamma-ray microcalorimeters were read out in 1 GHz of bandwidth in the initial demonstration. The system is used to perform high-resolution gamma-ray spectroscopy of samples of nuclear materials. To appropriately sample the microcalorimeter pulses, the resonators were designed to have bandwidths

of 300 kHz at a spacing of 3 MHz. The typical readout noise is approximately $30 \text{ pA}/\sqrt{\text{Hz}}$, a factor of ~ 5 below the noise of the TES. The pixel count has since been expanded to 256.

A large X-ray spectrometer is presently being assembled at NIST as part of the TOMCAT tomographic imaging system (Szypryt et al. 2021a), which has demonstrated readout of ~ 1000 detectors and will expand to 3000 detectors in the near future. To match the $\sim 1 \text{ A s}^{-1}$ slew rate of the detectors, the resonators have bandwidths of 1 MHz on a 7.5 MHz spacing. The detector assembly utilizes multiple modular “microsnouts” (Fig. 18), with 248 detectors per microsnout in 2 GHz of bandwidth.

Most relevant to the topic of cryogenic X-ray imaging spectrometers for astronomy is that μmux readout has been proposed for the Lynx LXM (Bandler et al. 2019) and the planning documents provide a useful guide to expected readout capability. The proposal calls for readout of $\sim 100,000$ pixels via a combination of thermal and electrical multiplexing, so that the main array would require 4,000 μmux channels with 1.4 MHz resonator bandwidths and 400 resonators per HEMT amplifier. Other sub-arrays have different readout requirements, which are laid out by Bandler et al. (2019) and Bennett et al. (2019). While Lynx is not yet a funded mission, technology advancement is ongoing to increase the readiness level of the readout and to simplify its application to future large-scale cryogenic X-ray astronomy instruments.

Summary and Future Prospects

The operation of large-scale arrays of cryogenic X-ray microcalorimeters in a satellite environment requires the minimization of heat loads and cryogenic complexity of the readout wiring. There are three main multiplexing technologies for accomplishing this: TDM, MHz-FDM, and μmux . All of these technologies are currently deployed to multiple ground-based instruments and planned for use in additional future satellite and ground-based instruments, as shown in Table 4.

In the near future, work on TDM will focus on the achievement of technology readiness level (TRL)-6 and beyond for Athena X-IFU. TRL-6 involves verification of the needed performance in a high-fidelity prototype that is tested in a relevant environment. The X-IFU Engineering Model (EM) is intended to provide such verification of all X-IFU systems. Aspects of TDM to be tested in the X-IFU EM will include a fully differential wiring architecture, X-IFU’s long cable harnesses and how they impact the open-loop bandwidth needed to operate with 160 ns row times, and the yield of the 50 mK TDM components. Beyond X-IFU, TDM may hybridized to μmux as discussed further below.

Future work on MHz-FDM will target increasing the multiplexing factor per column, via narrowing the detector bandwidth without losing performance, increasing the upper limit of the usable bandwidth, and stabilizing the TES performance under high-frequency ac bias (see also Gottardi and Smith in this book for the state-of-the-art single-pixel performance under ac bias). It will also require improvements to the

Table 4 An overview of missions that have flown (upper section) or will fly/employ (lower section) cryogenic X-ray spectrometers

Mission	Launch date	Detector	Total # of sensors	Readout type	# of sensors per readout
XQC (McCammon et al. 2002)	2002	Semiconductor	18	JFET	1
Hitomi/SXS (Mitsuda et al. 2014)	2016	Semiconductor	36	JFET	1
Micro-X (Adams et al. 2020)	2018, 2022	TES	128	TDM	16
XRISM/Resolve (Ishisaki et al. 2018)	2023	Semiconductor	36	JFET	1
Athena/X-IFU (Barret et al. 2018)	Mid-2030s	TES	~2,500	TDM	33
BabyIAXO ^a (Abeln et al. 2021)	2025	MMC	TBD	μ mux	NA
HUBS ^a (Cui et al. 2020)	~2030	TES	~3,500	TDM or FDM	TBD
LEM ^a	Mid-2030s	TES	~14,000	TDM	60
Lynx ^a (Bandler et al. 2019; Stevenson et al. 2019)	Early 2040s	TES or MMC	~100,000	μ mux	TBD
Super-DIOS ^a (Sato et al. 2020)	Early 2040s	TES	~30,000	μ mux	~400

^aMissions in the conceptual or proposing phase

firmware and electronics to realize a lower-mass and simpler system. A multiplexing factor of ~ 50 to 60 seems feasible improvement in the near future (Vaccaro et al. 2022a). In parallel, the linearity of the energy-gain scale will be demonstrated in a full spectrometer under multi-column readout.

Future work on μ mux will continue to advance its technological readiness to match TDM and MHz-FDM. It will also attempt to improve fabrication capability to reliably achieve Q_i values above 200,000 and to define resonance frequencies more accurately than $\pm 0.02\%$, as well as improve consistency of the fabrication quality and yield. Finally, it will require a microwave packaging solution (e.g., bump-bonded unit cells that confine the microwave fields) that allows it to be readily integrated into a TES focal plane without risking degradation of microwave performance.

For space and ground projects, TDM and FDM are planned for arrays of up to about 10^4 pixels, while μ mux is planned for arrays of more than 10^4 pixels (or for smaller arrays of very fast detectors). However, while μ mux provides multiple gigahertz of output bandwidth, because of the current limitations on quality factor and frequency placement, it is difficult to optimize for very large numbers ($> 2,000$)

of low-bandwidth input signals. The bandwidth-utilization efficiency of μ mux with resonator bandwidths of greater than ~ 300 kHz is comparable to that of TDM and MHz-FDM, but it cannot maintain that efficiency for slower input signals that require bandwidths narrower than can currently be fabricated.

For this reason, several groups have begun working on hybrid multiplexing solutions (Schuster et al. 2022; Yu et al. 2020), in which TDM, CDM, or MHz-FDM are used as a front end to combine multiple slow input signals into a single μ mux “pixel.” These hybrid solutions could potentially enable multiplexing factors in the tens of thousands, which will probably be necessary for instruments measuring faint astronomical X-ray objects, in which the optimization will tend toward large (megapixel-scale) arrays of slow TESs to tile the focal plane.

The development time for new technologies to be space ready is about 20 to 30 years, as seen in the gap between terrestrial and space projects in Fig. 23. Beyond X-ray astronomy, these developments will also have terrestrial X-ray spectroscopic applications in basic physics and materials analysis.

Cross-References

- [Transition-Edge Sensors for Cryogenic X-ray Imaging Spectrometers](#)

References

- K.O. Abazajian CMB-S4: forecasting constraints on primordial gravitational waves. *Astrophys. J.* **926**(1), 54 (2022). <https://doi.org/10.3847/1538-4357/ac1596>, 2008.12619
- A. Abeln et al., Conceptual design of babyIAXO, the intermediate stage towards the international axion observatory. *J. High Energy. Phys.* **2021**(5), 1–80 (2021)
- J.S. Adams et al., First operation of TES microcalorimeters in space with the Micro-X sounding rocket. *J. Low Temp. Phys.* **199**(3–4), 1062–1071 (2020). <https://doi.org/10.1007/s10909-019-02293-5>, 1908.09689
- J.S. Adams et al., First operation of transition-edge sensors in space with the Micro-X sounding rocket, in *X-ray, Optical, and Infrared Detectors for Astronomy IX*, ed. by A.D. Holland, J. Beletic. International Society for Optics and Photonics, SPIE, vol. 11454 (2021), pp. 195–203. <https://doi.org/10.1117/12.2562645>
- P. Ade et al., The simons observatory: science goals and forecasts. *J. Cosmol. Astropart. Phys.* **2019**(2), 056 (2019). <https://doi.org/10.1088/1475-7516/2019/02/056>, 1808.07445
- F. Ahrens, M. Wegner, P. Paluch, A. Fleischmann, C. Enss, S. Kempf, Superconducting GHz resonators for microwave SQUID multiplexing of metallic magnetic calorimeters. *Verhandlungen der Deutschen Physikalischen Gesellschaft* (2019)
- H. Akamatsu et al., Performance of TES X-ray microcalorimeters with AC bias read-out at MHz frequencies. *J. Low Temp. Phys.* **176**, 591–596 (2014). <https://doi.org/10.1007/s10909-014-1130-8>
- H. Akamatsu et al., Progress in the development of frequency-domain multiplexing for the X-ray integral field unit on board the athena mission. *J. Low Temp. Phys.* **199**(3–4), 737–744 (2020). <https://doi.org/10.1007/s10909-020-02351-3>

- H. Akamatsu et al., Demonstration of MHz frequency domain multiplexing readout of 37 transition edge sensors for high-resolution X-ray imaging spectrometers. *Appl. Phys. Lett.* **119**(18), 182601 (2021). <https://doi.org/10.1063/5.0066240>, 2111.01797
- P.W. Anderson, J.M. Rowell, Probable observation of the Josephson superconducting tunneling effect. *PRL* **10**(6), 230–232 (1963). <https://doi.org/10.1103/PhysRevLett.10.230>
- J.E. Austermann, SPTpol: an instrument for CMB polarization measurements with the South Pole Telescope, in *Millimeter, Submillimeter, and Far-Infrared Detectors and Instrumentation for Astronomy VI*, ed. by W.S. Holland, J. Zmuidzinas. Society of Photo-Optical Instrumentation Engineers (SPIE) Conference Series, vol. 8452 (2012), p. 84521E. <https://doi.org/10.1117/12.927286>, 1210.4970
- S.R. Bandler et al., Lynx X-ray microcalorimeter. *J. Astron. Telesc. Instrum. Syst.* **5**, 021017 (2019). <https://doi.org/10.1117/1.JATIS.5.2.021017>
- D. Barret et al., The ATHENA X-ray integral field unit (X-IFU), in *SPIE*. Society of Photo-Optical Instrumentation Engineers (SPIE) Conference Series, vol. 10699 (2018), p. 106991G. <https://doi.org/10.1117/12.2312409>
- E.S. Battistelli et al., Functional description of read-out electronics for time-domain multiplexed bolometers for millimeter and sub-millimeter astronomy. *J. Low Temp. Phys.* **151**(3), 908–914 (2008)
- D.J. Benford, First astronomical use of multiplexed transition edge bolometers, in *Low Temperature Detectors*, ed. by F.S. Porter, D. McCammon, M. Galeazzi, C.K. Stahle. American Institute of Physics Conference Series, vol. 605 (2002), pp. 589–592. <https://doi.org/10.1063/1.1457715>
- D.A. Bennett, J.A. Mates, S.R. Bandler et al., Microwave SQUID multiplexing for the Lynx X-ray microcalorimeter. *J. Astron. Telesc. Instrum. Syst.* **5**(2), 021007 (2002)
- D.A. Bennett et al., A high resolution gamma-ray spectrometer based on superconducting microcalorimeters. *Rev. Sci. Instrum.* **83**(9), 093113 (2012)
- D.A. Bennett et al., Integration of TES microcalorimeters with microwave SQUID multiplexed readout. *IEEE Trans. Appl. Supercond.* **25**(3), 1–5 (2014)
- A. Bergen et al., Design and validation of a large-format transition edge sensor array magnetic shielding system for space application. *Rev. Sci. Instrum.* **87**(10), 105109 (2016). <https://doi.org/10.1063/1.4962157>
- J. Beyer, D. Drung, A SQUID multiplexer with superconducting-to-normalconducting switches. *Supercond. Sci. Technol.* **21**(10), 105022 (2008)
- M.P. Bruijn et al., Tailoring the high-Q LC filter arrays for readout of kilo-pixel TES arrays in the SPICA-SAFARI instrument. *J. Low Temp. Phys.* **176**(3–4), 421–425 (2014). <https://doi.org/10.1007/s10909-013-1003-6>
- M.P. Bruijn et al., LC filters for FDM readout of the X-IFU TES calorimeter instrument on athena. *J. Low Temp. Phys.* **193**(5–6), 661–667 (2018). <https://doi.org/10.1007/s10909-018-1951-y>
- W. Cash, Parameter estimation in astronomy through application of the likelihood ratio. *Astrophys. J.* **228**, 939–947 (1979). <https://doi.org/10.1086/156922>
- J.A. Chervenak et al., Superconducting multiplexer for arrays of transition edge sensors. *Appl. Phys. Lett.* **74**(26), 4043 (1999). <https://doi.org/10.1063/1.123255>
- J.A. Chervenak et al., Superconducting multiplexer for arrays of transition edge sensors. *Appl. Phys. Lett.* **74**(26), 4043–4045 (1999)
- B. Chesca, R. Kleiner, D. Koelle, *SQUID Theory*, chap 2 (Wiley, 2004), pp. 29–92. <https://doi.org/10.1002/3527603646.ch2>
- D. Cohen, E. Givler, Magnetomyography: magnetic fields around the human body produced by skeletal muscles. *Appl. Phys. Lett.* **21**(3), 114–116 (1972). <https://doi.org/10.1063/1.1654294>
- W. Cui et al., HUBS: a dedicated hot circumgalactic medium explorer, in *Society of Photo-Optical Instrumentation Engineers (SPIE) Conference Series*, vol. 11444 (2020), p. 114442S. <https://doi.org/10.1117/12.2560871>
- M.F. Cunningham et al., High-resolution operation of frequency-multiplexed transition-edge photon sensors. *Appl. Phys. Lett.* **81**(1), 159 (2002). <https://doi.org/10.1063/1.1489486>

- M. D'Andrea et al., The cryogenic anticoincidence detector for ATHENA X-IFU: a scientific assessment of the observational capabilities in the hard X-ray band. *Exp. Astron.* **44**(3), 359–370 (2017). <https://doi.org/10.1007/s10686-017-9543-4>
- M. D'Andrea et al., The demonstration model of the ATHENA X-IFU cryogenic anticoincidence detector. *J. Low Temp. Phys.* **199**(1–2), 65–72 (2020). <https://doi.org/10.1007/s10909-019-02300-9>
- M. D'Andrea et al., Single pixel performance of a 32×32 Ti/Au TES array with broadband X-ray spectra. *IEEE Trans. Appl. Supercond.* **31**(5), 3065303 (2021). <https://doi.org/10.1109/TASC.2021.3065303>
- C.S. Dawson et al., Two-level switches for advanced time-division multiplexing. *IEEE Trans. Appl. Supercond.* **29**(5), 2500205 (2019)
- T. de Haan, G. Smecher, M. Dobbs, Improved performance of TES bolometers using digital feedback, in *Millimeter, Submillimeter, and Far-Infrared Detectors and Instrumentation for Astronomy VI*, ed. by W.S. Holland, J. Zmuidzinas. Society of Photo-Optical Instrumentation Engineers (SPIE) Conference Series, vol. 8452 (2012), p. 84520E. <https://doi.org/10.1117/12.925658>
- T. de Haan et al., Recent advances in frequency-multiplexed TES readout: vastly reduced parasitics and an increase in multiplexing factor with sub-kelvin SQUIDS. *J. Low Temp. Phys.* **199**(3–4), 754–761 (2020). <https://doi.org/10.1007/s10909-020-02403-8>
- M. de Wit et al., Performance of the SRON Ti/Au transition edge sensor X-ray calorimeters (2022). arXiv e-prints arXiv:2208.12556, 2208.12556
- R. den Hartog et al., Baseband feedback for frequency-domain-multiplexed readout of TES X-ray detectors, in *American Institute of Physics Conference Series*, vol. 1185, ed. by B. Young, B. Cabrera, A. Miller (2009), pp. 261–264. <https://doi.org/10.1063/1.3292328>
- R. den Hartog et al., Performance of a state-of-the-art DAC system for FDM readout, in *Space Telescopes and Instrumentation 2018: Ultraviolet to Gamma Ray*, ed. by J.W.A. den Herder, S. Nikzad, K. Nakazawa. Society of Photo-Optical Instrumentation Engineers (SPIE) Conference Series, vol. 10699 (2018), p. 106994Q. <https://doi.org/10.1117/12.2312793>
- J.W. den Herder et al., The reflection grating spectrometer on board XMM-Newton. *Astron. Astrophys.* **365**, L7–L17 (2001). <https://doi.org/10.1051/0004-6361:20000058>
- S.R.O. Dicker, A 90-GHz bolometer array for the Green Bank Telescope, in *Society of Photo-Optical Instrumentation Engineers (SPIE) Conference Series*, vol. 6275, ed. by J. Zmuidzinas, W.S. Holland, S. Withington, W.D. Duncan (2006), p. 62751B. <https://doi.org/10.1117/12.672166>
- S.R. Dicker, MUSTANG2: a large focal plan array for the 100 meter green bank telescope, in *Millimeter, Submillimeter, and Far-Infrared Detectors and Instrumentation for Astronomy VII*, ed. by W.S. Holland, J. Zmuidzinas. Society of Photo-Optical Instrumentation Engineers (SPIE) Conference Series, vol. 9153 (2014), p. 91530J. <https://doi.org/10.1117/12.2056455>
- M. Dobbs, E. Bissonnette, H. Spieler, Digital frequency domain multiplexer for millimeter-wavelength telescopes. *IEEE Trans. Nucl. Sci.* **55**(1), 21–26 (2008). <https://doi.org/10.1109/TNS.2007.911601>
- W.B. Doriese et al., Progress toward kilopixel arrays: 3.8 eV microcalorimeter resolution in 8-channel SQUID multiplexer. *Nucl. Instrum. Methods Phys. Res. Sect. A: Accel. Spectrom. Detect. Assoc. Equip.* **559**(2), 808–810 (2006)
- W.B. Doriese et al., Developments in time-division multiplexing of X-ray transition-edge sensors. *J. Low Temp. Phys.* **184**(1), 389–395 (2016)
- W.B. Doriese et al., A practical superconducting-microcalorimeter X-ray spectrometer for beam-line and laboratory science. *Rev. Sci. Instrum.* **88**(5), 053108 (2017)
- W.B. Doriese et al., Optimization of time-and code-division-multiplexed readout for athena x-ifu. *IEEE Trans. Appl. Supercond.* **29**(5), 2500305 (2019)
- D. Drung et al., DC SQUID readout electronics with up to 100 MHz closed-loop bandwidth. *IEEE Trans. Appl. Supercond.* **15**(2), 777–780 (2005)

- D. Drung et al., Highly sensitive and easy-to-use SQUID sensors. *IEEE Trans. Appl. Supercond.* **17**(2), 699–704 (2007). <https://doi.org/10.1109/TASC.2007.897403>
- K.G. Duh et al., Ultra-low-noise cryogenic high-electron-mobility transistors. *IEEE Trans. Electron Dev.* **35**(3), 249–256 (1988)
- M. Durkin et al., Demonstration of athena X-IFU compatible 40-row time-division-multiplexed readout. *IEEE Trans. Appl. Supercond.* **29**(5), 2904472 (2019). <https://doi.org/10.1109/TASC.2019.2904472>
- M. Durkin et al., A predictive control algorithm for time-division-multiplexed readout of TES microcalorimeters. *J. Low Temp. Phys.* **199**(1–2), 275–280 (2020). <https://doi.org/10.1007/s10909-020-02342-4>
- M. Durkin et al., Mitigation of finite bandwidth effects in time-division-multiplexed SQUID readout of TES arrays. *IEEE Trans. Appl. Supercond.* **31**(5), 1600905 (2021)
- A. Fleischmann, C. Enss, G. Seidel, *Metallic Magnetic Calorimeters* (Springer, Berlin, Heidelberg, 2005), pp. 151–216
- J.W. Fowler et al., Absolute energies and emission line shapes of the L X-ray transitions of lanthanide metals. *Metrologia* **58**(1), 015016 (2021)
- S. Friedrich, Cryogenic X-ray detectors for synchrotron science. *J. Synchrotron Radiat.* **13**(2), 159–171 (2006)
- N.N. Gandilo et al., The primordial inflation polarization explorer (PIPER), in *Millimeter, Submillimeter, and Far-Infrared Detectors and Instrumentation for Astronomy VIII*, vol. 9914 (2006), pp. 372–379
- J. Gao et al., Experimental evidence for a surface distribution of two-level systems in superconducting lithographed microwave resonators. *Appl. Phys. Lett.* **92**(15), 152505 (2008)
- M. Gonzales et al., Fully differential broadband LNA with active impedance matching for SQUID readout. *J. Low Temp. Phys.* p in review
- L. Gottardi, K. Nagayashi, A review of X-ray microcalorimeters based on superconducting transition edge sensors for astrophysics and particle physics. *Appl. Sci.* **11**(9), (2021). <https://doi.org/10.3390/app11093793>, <https://www.mdpi.com/2076-3417/11/9/3793>
- L. Gottardi et al., Josephson effects in an alternating current biased transition edge sensor. *Appl. Phys. Lett.* **105**(16), 162605 (2014a). <https://doi.org/10.1063/1.4899065>
- L. Gottardi et al., Weak-link phenomena in AC-biased transition edge sensors. *J. Low Temp. Phys.* **176**, 279–284 (2014b). <https://doi.org/10.1007/s10909-014-1093-9>
- L. Gottardi et al., Josephson effects in frequency-domain multiplexed TES microcalorimeters and bolometers. *J. Low Temp. Phys.* **193**(3–4), 209–216 (2018). <https://doi.org/10.1007/s10909-018-2006-0>
- L. Gottardi et al., A six-degree-of-freedom micro-vibration acoustic isolator for low-temperature radiation detectors based on superconducting transition-edge sensors. *Rev. Sci. Instrum.* **90**(5), 055107 (2019). <https://doi.org/10.1063/1.5088364>
- E. Grace, ACTPol: on-sky performance and characterization, in *Millimeter, Submillimeter, and Far-Infrared Detectors and Instrumentation for Astronomy VII*, ed. by W.S. Holland, J. Zmuidzinas. Society of Photo-Optical Instrumentation Engineers (SPIE) Conference Series, vol. 9153 (2014), p. 915310. <https://doi.org/10.1117/12.2057243>
- D.A. Harper et al., HAWC+, the far-infrared camera and polarimeter for sofia. *J. Astron. Instrum.* **7**(04), 1840008 (2018)
- T. Hashimoto et al., Measurements of strong-interaction effects in kaonic-helium isotopes at sub-eV precision with X-ray microcalorimeters. *Phys. Rev. Lett.* **128**(11), 112503 (2022)
- M. Hazumi et al., LiteBIRD satellite: JAXA's new strategic L-class mission for all-sky surveys of cosmic microwave background polarization, in *Society of Photo-Optical Instrumentation Engineers (SPIE) Conference Series*, vol. 11443 (2020), p. 114432F. <https://doi.org/10.1117/12.2563050>
- S.W. Henderson, Advanced ACTPol cryogenic detector arrays and readout. *J. Low Temp. Phys.* **184**(3–4), 772–779 (2016)
- J. Henning, SPT-3G: the third generation camera and survey for the south pole telescope, in *American Astronomical Society Meeting Abstracts*, vol. 225 (2015), p. 220.02

- F. Hirayama et al., Microwave SQUID multiplexer for TES readout. *IEEE Trans. Appl. Supercond.* **23**(3), 2500405–2500405 (2013)
- Hitomi Collaboration et al., The quiescent intracluster medium in the core of the Perseus cluster. *Nature* **535**(7610), 117–121 (2016). <https://doi.org/10.1038/nature18627>
- W.S. Holland et al., SCUBA-2: the 10,000 pixel bolometer camera on the James Clerk Maxwell telescope. *Mon. Not. R. Astron. Soc.* **430**(4), 2513–2533 (2013)
- G. Hölzer et al., $K\alpha_{1,2}$ and $K\beta_{1,3}$ X-ray emission lines of the 3d transition metals. *Phys. Rev. A* **56**(6), 4554–4568 (1997). <https://doi.org/10.1103/PhysRevA.56.4554>
- M.E. Huber et al., DC SQUID series arrays with intracoil damping to reduce resonance distortions. *Appl. Supercond.* **5**(7–12), 425–429 (1997)
- M.E. Huber et al., DC SQUID series array amplifiers with 120 MHz bandwidth (corrected). *IEEE Trans. Appl. Supercond.* **11**(2), 4048–4053 (2001)
- Y. Inoue, POLARBEAR-2: an instrument for CMB polarization measurements, in *Millimeter, Submillimeter, and Far-Infrared Detectors and Instrumentation for Astronomy VIII*, ed. by W.S. Holland, J. Zmuidzinas. Society of Photo-Optical Instrumentation Engineers (SPIE) Conference Series, vol. 9914 (2016), p. 99141I. <https://doi.org/10.1117/12.2231961>, 1608.03025
- K.D. Irwin, An application of electrothermal feedback for high resolution cryogenic particle detection. *Appl. Phys. Lett.* **66**(15), 1998–2000 (1995). <https://doi.org/10.1063/1.113674>
- K.D. Irwin, Shannon limits for low-temperature detector readout, in *The Thirteenth International Workshop on Low Temperature Detectors – LTD13*, ed. by B. Young, B. Cabrera, A. Miller. American Institute of Physics Conference Series, vol. 1185 (2009), pp. 229–236. <https://doi.org/10.1063/1.3292320>
- K.D. Irwin, G.C. Hilton, *Transition-Edge Sensors* (Springer, Berlin, Heidelberg, 2005) pp. 63–150
- K.D. Irwin, K.W. Lehnert, Microwave SQUID multiplexer. *Appl. Phys. Lett.* **85**(11), 2107 (2004). <https://doi.org/10.1063/1.1791733>
- K.D. Irwin et al., Code-division multiplexing of superconducting transition-edge sensor arrays. *Supercond. Sci. Technol.* **23**(3), 034004 (2010). <https://doi.org/10.1088/0953-2048/23/3/034004>
- K.D. Irwin et al., Advanced code-division multiplexers for superconducting detector arrays. *J. Low Temp. Phys.* **167**(5), 588–594 (2012)
- Y. Ishisaki et al., Resolve instrument on X-ray Astronomy Recovery Mission (XARM). *J. Low Temp. Phys.* **193**(5–6), 991–995 (2018). <https://doi.org/10.1007/s10909-018-1913-4>
- B.D. Jackson et al., The focal plane assembly for the Athena X-ray Integral Field Unit instrument, in *Space Telescopes and Instrumentation 2016: Ultraviolet to Gamma Ray*, ed. by J.W.A. den Herder, T. Takahashi, M. Bautz. Society of Photo-Optical Instrumentation Engineers (SPIE) Conference Series, vol. 9905 (2016), p. 99052I. <https://doi.org/10.1117/12.2232544>
- R.C. Jaklevic et al., Quantum interference effects in Josephson tunneling. *PRL* **12**(7), 159–160 (1964). <https://doi.org/10.1103/PhysRevLett.12.159>
- J.S. Kaastra, J.A.M. Bleeker, Optimal binning of X-ray spectra and response matrix design. *Astron. Astrophys.* **587**, A151 (2016). <https://doi.org/10.1051/0004-6361/201527395>, 1601.05309
- R.L. Kelley et al., The Suzaku high resolution X-ray spectrometer. *Publ. Astron. Soc. Jpn.* **59**, 77–112 (2007). <https://doi.org/10.1093/pasj/59.sp1.S77>
- R.L. Kelley et al., Ion-implanted silicon X-ray calorimeters: present and future. *J. Low Temp. Phys.* **151**(1–2), 375–380 (2008). <https://doi.org/10.1007/s10909-007-9663-8>
- S. Kempf et al., Physics and applications of metallic magnetic calorimeters. *J. Low Temp. Phys.* **193**(3–4), 365–379 (2018). <https://doi.org/10.1007/s10909-018-1891-6>
- Z. Kermish, The POLARBEAR experiment, in *Millimeter, Submillimeter, and Far-Infrared Detectors and Instrumentation for Astronomy VI*, ed. by W.S. Holland, J. Zmuidzinas. Society of Photo-Optical Instrumentation Engineers (SPIE) Conference Series, vol. 8452 (2012), p. 84521C. <https://doi.org/10.1117/12.926354>, 1210.7768
- S. Kimura et al., Performance measurement of the 8-Input SQUIDS for TES frequency domain multiplexing. *J. Low Temp. Phys.* **151**(3–4), 946–951 (2008). <https://doi.org/10.1007/s10909-008-9771-0>

- M. Kiviranta, L. Grönberg, J. van der Kuur, Two SQUID amplifiers intended to alleviate the summing node inductance problem in multiplexed arrays of Transition Edge Sensors (2018). arXiv e-prints arXiv:1810.09122
- M. Kiviranta et al., SQUID-based readout schemes for microcalorimeter arrays, in *Low Temperature Detectors*, ed. by F.S. Porter, D. McCammon, M. Galeazzi, C.K. Stahle. American Institute of Physics Conference Series, vol. 605 (2002), pp. 295–300. <https://doi.org/10.1063/1.1457649>
- M. Kiviranta et al., Design and performance of multiloop and washer SQUIDs intended for sub-kelvin operation. *Supercond. Sci. Technol.* **17**(5), S285–S289 (2004). <https://doi.org/10.1088/0953-2048/17/5/038>
- M. Kiviranta et al., Two-stage SQUID amplifier for the frequency multiplexed readout of the X-IFU X-ray camera. *IEEE Trans. Appl. Supercond.* **31**(5), 3060356 (2021). <https://doi.org/10.1109/TASC.2021.3060356>
- S. Lee et al., (2022) Generic character of charge and spin density waves in superconducting cuprates. *Proc. Natl. Acad. Sci.* **119**(15), e2119429119 (2022)
- S.J. Lee et al., Soft X-ray spectroscopy with transition-edge sensors at stanford synchrotron radiation lightsource beamline 10–1. *Rev. Sci. Instrum.* **90**(11), 113101 (2019). <https://doi.org/10.1063/1.5119155>
- K.K. Likharev, *Dynamics of Josephson Junctions and Circuits* p 640, (Routledge, 2022)
- T.J. Lucas et al., Indium bump process for low-temperature detectors and readout. *J. Low Temp. Phys.* **209**(3–4), 293–298 (2022)
- C. Macculi C et al., The Cryogenic AntiCoincidence detector for ATHENA X-IFU: a program overview, in *Space Telescopes and Instrumentation 2016: Ultraviolet to Gamma Ray*, ed. by J.W.A. den Herder, T. Takahashi, M. Bautz. Society of Photo-Optical Instrumentation Engineers (SPIE) Conference Series, vol. 9905 (2016), p. 99052K. <https://doi.org/10.1117/12.2231298>
- M. Malnou et al., Performance of a kinetic inductance traveling-wave parametric amplifier at 4 kelvin: toward an alternative to semiconductor amplifiers. *Phys. Rev. Appl.* **17**(4), 044009 (2022)
- F. Mantegazzini et al., Metallic magnetic calorimeter arrays for the first phase of the ECHO experiment. *Nucl. Instrum. Methods Phys. Res. A* **1030**, 166406 (2022). <https://doi.org/10.1016/j.nima.2022.166406>, 2111.09945
- T.H. Markert et al., High-energy transmission grating spectrometer for the Advanced X-ray Astrophysics Facility (AXAF), in *EUV, X-ray, and Gamma-Ray Instrumentation for Astronomy V*, ed. by O.H. Siegmund, J.V. Vallerga. Society of Photo-Optical Instrumentation Engineers (SPIE) Conference Series, vol. 2280 (1994), pp. 168–180. <https://doi.org/10.1117/12.186812>
- J. Mates et al., Demonstration of a multiplexer of dissipationless superconducting quantum interference devices. *Appl. Phys. Lett.* **92**(2), 023514 (2008)
- J. Mates et al., Flux-ramp modulation for SQUID multiplexing. *J. Low Temp. Phys.* **167**(5), 707–712 (2012)
- J. Mates et al., Simultaneous readout of 128 X-ray and gamma-ray transition-edge microcalorimeters using microwave SQUID multiplexing. *Appl. Phys. Lett.* **111**(6), 062601 (2017)
- J. Mates et al., Crosstalk in microwave SQUID multiplexers. *Appl. Phys. Lett.* **115**(20), 202601 (2019)
- J.A.B. Mates, The microwave SQUID multiplexer. PhD thesis, 2011
- D. McCammon, *Semiconductor Thermistors* (Springer, Berlin, Heidelberg, 2005), pp. 35–62
- D. McCammon, *Thermal Equilibrium Calorimeters - An Introduction*, vol. 99 (Springer, Berlin, Heidelberg, 2005), p. 1
- D. McCammon et al., A high spectral resolution observation of the soft X-ray diffuse background with thermal detectors. *Astrophys. J.* **576**(1), 188–203 (2002). <https://doi.org/10.1086/341727>
- J. Mehl, TES bolometer array for the APEX-SZ camera. *J. Low Temp. Phys.* **151**(3–4), 697–702 (2008). <https://doi.org/10.1007/s10909-008-9738-1>
- L. Míajaja-Avila et al., Ultrafast time-resolved hard X-ray emission spectroscopy on a tabletop. *Phys. Rev. X* **6**, 031047 (2016)

- K. Mitsuda et al., Multi-pixel readout of transition-edge sensors using a multi-input SQUID. *Nucl. Instrum. Methods Phys. Res A* **436**(1–2), 252–255 (1999). [https://doi.org/10.1016/S0168-9002\(99\)00630-0](https://doi.org/10.1016/S0168-9002(99)00630-0)
- K. Mitsuda et al., The X-ray observatory Suzaku. *Publ. Astron. Soc. Jpn.* **59**, 1–7 (2007). <https://doi.org/10.1093/pasj/59.sp1.S1>
- K. Mitsuda et al., Soft X-ray spectrometer (SXS): the high-resolution cryogenic spectrometer onboard ASTRO-H, in *Space Telescopes and Instrumentation 2014: Ultraviolet to Gamma Ray*, ed. by T. Takahashi, J.W.A. den Herder, M. Bautz. Society of Photo-Optical Instrumentation Engineers (SPIE) Conference Series, vol. 9144 (2014), p. 91442A. <https://doi.org/10.1117/12.2057199>
- J. Montgomery et al., Performance and characterization of the SPT-3G digital frequency-domain multiplexed readout system using an improved noise and crosstalk model. *J. Astron. Telesc. Instrum. Syst.* **8**(1), 014001 (2022). <https://doi.org/10.1117/1.JATIS.8.1.014001>, 2103.16017
- K.M. Morgan et al., Code-division-multiplexed readout of large arrays of TES microcalorimeters. *Appl. Phys. Lett.* **109**(11), 112604 (2016). <https://doi.org/10.1063/1.4962636>
- S.H. Moseley, J.C. Mather, D. McCammon, Thermal detectors as X-ray spectrometers. *J. Appl. Phys.* **56**(5), 1257–1262 (1984). <https://doi.org/10.1063/1.334129>
- K. Nagayoshi et al., Development of a Ti/Au TES microcalorimeter array as a backup sensor for the Athena/X-IFU instrument. *J. Low Temp. Phys.* **199**(3–4), 943–948 (2020). <https://doi.org/10.1007/s10909-019-02282-8>
- Y. Nakashima et al., Low-noise microwave SQUID multiplexed readout of 38 X-ray transition-edge sensor microcalorimeters. *Appl. Phys. Lett.* **117**(12), 122601 (2020). <https://doi.org/10.1063/5.0016333>
- O. Noroozian et al., Crosstalk reduction for superconducting microwave resonator arrays. *IEEE Trans. Microwave Theory Tech.* **60**(5), 1235–1243 (2012)
- T. Okumura et al., Deexcitation dynamics of muonic atoms revealed by high-precision spectroscopy of electronic k X-rays. *Phys. Rev. Lett.* **127**(5), 053001 (2021)
- G.C. O’Neil et al., Ultrafast time-resolved X-ray absorption spectroscopy of ferrioxalate photolysis with a laser plasma X-ray source and microcalorimeter array. *J. Phys. Chem. Lett.* **8**(5), 1099–1104 (2017)
- BICEP2 collaboration and others, Detection of B-mode polarization at degree angular scales by BICEP2. *PRL* **112**(24), 241101 (2014). <https://doi.org/10.1103/PhysRevLett.112.241101>, 1403.3985
- LiteBIRD collaboration and others, Probing Cosmic Inflation with the LiteBIRD Cosmic Microwave Background Polarization Survey (2022). arXiv e-prints arXiv:2202.02773, 2202.02773
- M.R.J. Palosaari et al., Broadband ultrahigh-resolution spectroscopy of particle-induced x rays: extending the limits of nondestructive analysis. *Phys. Rev. Appl.* **6**(2), 024002 (2016)
- F.S. Porter et al., The astro-H soft X-ray spectrometer (SXS), in *The Thirteenth International Workshop on Low Temperature Detectors – LTD13*, ed. by B. Young, B. Cabrera, A. Miller. American Institute of Physics Conference Series, vol. 1185 (2009), pp. 91–94. <https://doi.org/10.1063/1.3292564>
- F.S. Porter et al., The detector subsystem for the SXS instrument on the ASTRO-H Observatory, in *Space Telescopes and Instrumentation 2010: Ultraviolet to Gamma Ray*, ed. by M. Arnaud, S.S. Murray, T. Takahashi. Society of Photo-Optical Instrumentation Engineers (SPIE) Conference Series, vol. 7732 (2010), p. 77323J. <https://doi.org/10.1117/12.857888>
- L. Ravera et al., The X-ray integral field unit (X-IFU) for Athena, in *Space Telescopes and Instrumentation 2014: Ultraviolet to Gamma Ray*, SPIE, vol. 9144 (2014), p. 91442L. <https://doi.org/10.1117/12.2055884>
- C.D. Reintsema et al., Prototype system for superconducting quantum interference device multiplexing of large-format transition-edge sensor arrays. *Rev. Sci. Instrum.* **74**(10), 4500–4508 (2003)

- C.D. Reintsema et al., Electronics for a next-generation SQUID-based time-domain multiplexing system, in *AIP Conference Proceedings*, vol. 1185 (2009), pp. 237–240
- P. Roelfsema et al., The SAFARI imaging spectrometer for the SPICA space observatory, in *Space Telescopes and Instrumentation 2012: Optical, Infrared, and Millimeter Wave*, ed. by M.C. Clampin, G.G. Fazio, H.A. MacEwen, J. Oschmann, M. Jacobus. Society of Photo-Optical Instrumentation Engineers (SPIE) Conference Series, vol. 8442 (2012), p. 84420R. <https://doi.org/10.1117/12.927010>
- J.E. Sadleir et al., Longitudinal proximity effects in superconducting transition-edge sensors. *PRL* **104**(4), 047003 (2010). <https://doi.org/10.1103/PhysRevLett.104.047003>
- J.E. Sadleir et al., Proximity effects and nonequilibrium superconductivity in transition-edge sensors. *PRB* **84**(18), 184502 (2011). <https://doi.org/10.1103/PhysRevB.84.184502>
- K. Sakai et al., Developments of laboratory-based transition-edge sensor readout electronics using commercial-off-the-shelf modules. *J. Low Temp. Phys.* p in review
- K. Sato et al., Super DIOS mission for exploring “dark baryon”, in *Society of Photo-Optical Instrumentation Engineers (SPIE) Conference Series*, vol. 11444 (2020), p. 114445O. <https://doi.org/10.1117/12.2561681>
- C. Schuster et al., Flux ramp modulation based hybrid microwave SQUID multiplexer. *Appl. Phys. Lett.* **120**(16), 162601 (2022)
- N. Sehgal, CMB-HD: an ultra-deep, high-resolution millimeter-wave survey over half the sky, in *Bulletin of the American Astronomical Society*, vol. 51 (2019), p. 6. 1906.10134
- S.J. Smith et al., Small pitch transition-edge sensors with broadband high spectral resolution for solar physics. *J. Low Temp. Phys.* **167**(3–4), 168–175 (2012). <https://doi.org/10.1007/s10909-012-0574-y>
- S.J. Smith et al., Toward 100,000-Pixel microcalorimeter arrays using multi-absorber transition-edge sensors. *J. Low Temp. Phys.* **199**(1–2), 330–338 (2020). <https://doi.org/10.1007/s10909-020-02362-0>
- S.J. Smith et al., Performance of a broad-band, high-resolution, transition-edge sensor spectrometer for X-ray astrophysics. *IEEE Trans. Appl. Supercond.* **31**(5), 2100806 (2021)
- T.R. Stevenson et al., Magnetic calorimeter option for the Lynx X-ray microcalorimeter. *J. Astron. Telesc. Instrum. Syst.* **5**(2), 1–9 (2019). <https://doi.org/10.1117/1.JATIS.5.2.021009>
- D.S. Swetz et al., Overview of the atacama cosmology telescope: receiver, instrumentation, and telescope systems. *Astrophys. J. Suppl. Ser.* **194**(2), 41 (2011). <https://doi.org/10.1088/0067-0049/194/2/41>
- P. Szypryt, D.A. Bennett et al., Design of a 3000-pixel transition-edge sensor X-ray spectrometer for microcircuit tomography. *IEEE Trans. Appl. Supercond.* **31**(5), 1–5 (2021a)
- P. Szypryt et al., A transition-edge sensor-based X-ray spectrometer for the study of highly charged ions at the national institute of standards and technology electron beam ion trap. *Rev. Sci. Instrum.* **90**(12), 123107 (2019)
- P. Szypryt et al., Design of a 3000-pixel transition-edge sensor X-ray spectrometer for microcircuit tomography. *IEEE Trans. Appl. Supercond.* **31**(5), 2100405 (2021b)
- P. Szypryt et al., A tabletop X-ray tomography instrument for nanometer-scale imaging: demonstration of the 1,000-element transition-edge sensor subarray. *IEEE Trans. Appl. Supercond.* (2022) (in preparation)
- T. Takahashi et al., The ASTRO-H X-ray observatory, in *Society of Photo-Optical Instrumentation Engineers (SPIE) Conference Series*, vol. 8443 (2012). <https://doi.org/10.1117/12.926190>
- Y. Takei et al., SQUID multiplexing using baseband feedback for space application of transition-edge sensor microcalorimeters. *Supercond. Sci. Technol.* **22**(11), 114008 (2009). <https://doi.org/10.1088/0953-2048/22/11/114008>
- Y. Takei et al., Vibration isolation system for cryocoolers of soft X-ray spectrometer on-board ASTRO-H (Hitomi). *J. Astron. Telesc. Instrum. Syst.* **4**, 011216 (2018). <https://doi.org/10.1117/1.JATIS.4.1.011216>
- E. Taralli et al., Characterization of high aspect-ratio TiAu TES X-ray microcalorimeter array under AC bias. *J. Low Temp. Phys.* **199**(1–2), 80–87 (2020). <https://doi.org/10.1007/s10909-019-02254-y>

- E. Taralli et al., Ti/Au TES 32×32 pixel array: uniformity, thermal crosstalk and performance at different X-ray energies. *IEEE Trans. Appl. Supercond.* **31**(5), 3061022 (2021). <https://doi.org/10.1109/TASC.2021.3061022>
- M. Tashiro et al., Concept of the X-ray astronomy recovery mission, in *SPIE. Society of Photo-Optical Instrumentation Engineers (SPIE) Conference Series*, vol. 10699 (2018), p. 1069922. <https://doi.org/10.1117/12.2309455>
- The Lynx Team, The Lynx Mission Concept Study Interim Report (2018). arXiv e-prints arXiv:1809.09642
- J. Uhlig et al., Table-top ultrafast X-ray microcalorimeter spectrometry for molecular structure. *Phys. Rev. Lett.* **110**, 138302 (2013)
- J.N. Ullom, D.A. Bennett, Review of superconducting transition-edge sensors for X-ray and gamma-ray spectroscopy. *Supercond. Sci. Technol.* **28**(8), 084003 (2015). <https://doi.org/10.1088/0953-2048/28/8/084003>
- J.N. Ullom et al., A frequency-domain read-out technique for large microcalorimeter arrays demonstrated using high-resolution γ -ray sensors. *IEEE Trans. Appl. Supercond.* **13**(2), 643–648 (2003). <https://doi.org/10.1109/TASC.2003.813981>
- D. Vaccaro et al., Frequency Shift Algorithm: Application to a Frequency-Domain Multiplexing Readout of X-ray Transition-Edge Sensor Microcalorimeters (2021). arXiv e-prints arXiv:2102.06092
- D. Vaccaro et al., Frequency domain multiplexing readout for large arrays of transition-edge sensors (2022a). arXiv e-prints arXiv:2208.12604, 2208.12604
- D. Vaccaro et al., Susceptibility study of TES micro-calorimeters for X-ray spectroscopy under FDM readout (2022b). arXiv e-prints arXiv:2208.10875, 2208.10875
- D. Vaccaro et al., Thermal crosstalk of X-ray transition-edge sensor micro-calorimeters under frequency domain multiplexing readout. *IEEE Trans. Appl. Supercond.* **32**(1), 3128710 (2022c). <https://doi.org/10.1109/TASC.2021.3128710>
- P. van der Hulst et al., Frequency shift algorithm: design of a baseband phase locked loop for frequency-domain multiplexing readout of X-ray transition-edge sensor microcalorimeters. *Rev. Sci. Instrum.* **92**(7), 073101 (2021). <https://doi.org/10.1063/5.0044968>
- J. van der Kuur et al., Implementation of frequency domain multiplexing in imaging arrays of microcalorimeters. *Nucl. Instrum. Methods Phys. Res. A* **520**(1–3), 551–554 (2004). <https://doi.org/10.1016/j.nima.2003.11.312>
- J. van der Kuur et al., Optimising the multiplex factor of the frequency domain multiplexed readout of the TES-based microcalorimeter imaging array for the X-IFU instrument on the Athena X-ray observatory, in *Space Telescopes and Instrumentation 2016: Ultraviolet to Gamma Ray*, ed. by J.W.A. den Herder, T. Takahashi, M. Bautz. Society of Photo-Optical Instrumentation Engineers (SPIE) Conference Series, vol. 9905 (2016), p. 99055R. <https://doi.org/10.1117/12.2232830>
- H.J. van Weers, Niobium flex cable for low temperature high density interconnects. *Cryogenics* **55**, 1–4 (2013). <https://doi.org/10.1016/j.cryogenics.2012.10.006>
- J.L. Walsh, A closed set of normal orthogonal functions. *Am. J. Math.* **45**(1), 5–24 (1923)
- Q. Wang et al., Noise measurements of a low-noise amplifier in the FDM readout system for SAFARI. *J. Low Temp. Phys.* **199**(3–4), 817–823 (2020). <https://doi.org/10.1007/s10909-019-02328-x>
- M. Wegner, C. Enss, S. Kempf, Analytical model of the readout power and SQUID hysteresis parameter dependence of the resonator characteristics of microwave SQUID multiplexers. *Supercond. Sci. Technol.* **35**(7), 075011 (2022)
- M. Wegner et al., Microwave squid multiplexing of metallic magnetic calorimeters: status of multiplexer performance and room-temperature readout electronics development. *J. Low Temp. Phys.* **193**(3–4), 462–475 (2018). <https://doi.org/10.1007/s10909-018-1878-3>
- R.P. Welty, J.M. Martinis, A series array of DC SQUIDs. *IEEE Trans. Magn.* **27**(2), 2924–2926 (1991)
- S. Yamada et al., Broadband high-energy resolution hard X-ray spectroscopy using transition edge sensors at spring-8. *Rev. Sci. Instrum.* **92**(1), 013103 (2021)

- J. Yoon et al., Single superconducting quantum interference device multiplexer for arrays of low-temperature sensors. *Appl. Phys. Lett.* **78**(3), 371 (2001). <https://doi.org/10.1063/1.1338963>
- W. Yoon et al., Toward large field-of-view high-resolution X-ray imaging spectrometers: microwave multiplexed readout of 28 TES microcalorimeters. *J. Low Temp. Phys.* **193**(3–4), 258–266 (2018). <https://doi.org/10.1007/s10909-018-1917-0>
- C. Yu et al., An impedance-modulated code-division microwave SQUID multiplexer. *Eng. Res. Exp.* **2**(1), 015011 (2020). <https://doi.org/10.1088/2631-8695/ab68a4>
- H. Zappe, Josephson quantum interference computer devices. *IEEE Trans. Magn.* **13**(1), 41–47 (1977)